



<b>Publication Year</b>	2021
<b>Acceptance in OA</b>	2022-01-05T10:03:15Z
<b>Title</b>	A universal relation between the properties of supermassive black holes, galaxies, and dark matter haloes
<b>Authors</b>	MARASCO, ANTONINO, CRESCI, GIOVANNI, Posti, L., Fraternali, F., MANNUCCI, FILIPPO, Marconi, Alessandro, BELFIORE, FRANCESCO MICHEL CONCETTO, Fall, S. M.
<b>Publisher's version (DOI)</b>	10.1093/mnras/stab2317
<b>Handle</b>	<a href="http://hdl.handle.net/20.500.12386/31312">http://hdl.handle.net/20.500.12386/31312</a>
<b>Journal</b>	MONTHLY NOTICES OF THE ROYAL ASTRONOMICAL SOCIETY
<b>Volume</b>	507

# A universal relation between the properties of supermassive black holes, galaxies, and dark matter haloes

A. Marasco<sup>1</sup>,<sup>\*</sup> G. Cresci,<sup>1</sup> L. Posti<sup>2</sup>, F. Fraternali,<sup>3</sup> F. Mannucci<sup>1</sup>, A. Marconi,<sup>1,4</sup> F. Belfiore<sup>1</sup> and S. M. Fall<sup>5</sup>

<sup>1</sup>INAF - Osservatorio Astrofisico di Arcetri, Largo E. Fermi 5, I-50127 Firenze, Italy

<sup>2</sup>Université de Strasbourg, CNRS UMR 7550, Observatoire astronomique de Strasbourg, 11 rue de l'Université, F-67000 Strasbourg, France

<sup>3</sup>Kapteyn Astronomical Institute, University of Groningen, Postbus 800, NL-9700 AV Groningen, the Netherlands

<sup>4</sup>Dipartimento di Fisica e Astronomia, Università di Firenze, Via G. Sansone 1, I-50019 Sesto Fiorentino (Firenze), Italy

<sup>5</sup>Space Telescope Science Institute, 3700 San Martin Drive, Baltimore, MD 21218, USA

Accepted 2021 August 3. Received 2021 July 29; in original form 2021 May 21

## ABSTRACT

We study the relations between the mass of the central black hole (BH)  $M_{\text{BH}}$ , the dark matter halo mass  $M_{\text{h}}$ , and the stellar-to-halo mass fraction  $f_{\star} \propto M_{\star}/M_{\text{h}}$  in a sample of 55 nearby galaxies with dynamically measured  $M_{\text{BH}} > 10^6 M_{\odot}$  and  $M_{\text{h}} > 5 \times 10^{11} M_{\odot}$ . The main improvement with respect to previous studies is that we consider both early- and late-type systems for which  $M_{\text{h}}$  is determined either from globular cluster dynamics or from spatially resolved rotation curves. Independently of their structural properties, galaxies in our sample build a well defined sequence in the  $M_{\text{BH}}-M_{\text{h}}-f_{\star}$  space. We find that: (i)  $M_{\text{h}}$  and  $M_{\text{BH}}$  strongly correlate with each other and anticorrelate with  $f_{\star}$ ; (ii) there is a break in the slope of the  $M_{\text{BH}}-M_{\text{h}}$  relation at  $M_{\text{h}}$  of  $10^{12} M_{\odot}$ , and in the  $f_{\star}-M_{\text{BH}}$  relation at  $M_{\text{BH}}$  of  $\sim 10^7 - 10^8 M_{\odot}$ ; (iii) at a fixed  $M_{\text{BH}}$ , galaxies with a larger  $f_{\star}$  tend to occupy lighter haloes and to have later morphological types. We show that the observed trends can be reproduced by a simple equilibrium model in the  $\Lambda$ CDM framework where galaxies smoothly accrete dark and baryonic matter at a cosmological rate, having their stellar and BH build-up regulated both by the cooling of the available gas reservoir and by the negative feedback from star formation and active galactic nuclei (AGNs). Feature (ii) arises as the BH population transits from a rapidly accreting phase to a more gentle and self-regulated growth, while scatter in the AGN feedback efficiency can account for feature (iii).

**Key words:** galaxies: evolution – galaxies: formation – galaxies: haloes – galaxies: structure – quasars: supermassive black holes.

## 1 INTRODUCTION

In a simplified theoretical framework, the build-up of galaxies can be thought as resulting from the competition between the ‘positive’ process of cooling and gravitational collapse of gas within the potential wells provided by dark matter haloes (White & Rees 1978), and a series of ‘negative’ mechanisms such as gas heating and subsequent expulsions caused by feedback from star formation (Larson 1974; Dekel & Silk 1986) and active galactic nuclei (AGNs; Silk & Rees 1998; Harrison 2017). This competition between inflows and outflows or, alternatively, cooling and heating, ultimately regulates the galaxy gas reservoir out of which stars form and supermassive black holes (BHs) grow. This simple framework is at the basis of several successful theoretical models of galaxy formation and evolution (e.g. Somerville et al. 2008; Bouché et al. 2010; Lilly et al. 2013; Behroozi et al. 2019).

The picture described above suggests the existence of three ‘leading characters’ playing a major role in the evolution of a galaxy, namely its dark matter halo, its stellar component and its BH. Their masses ( $M_{\text{h}}$ ,  $M_{\star}$ , and  $M_{\text{BH}}$ ) and growth rates are closely related to

the positive and negative processes discussed: gas accretes on to haloes at rates of  $f_{\text{b}}\dot{M}_{\text{h}}$  ( $f_{\text{b}}$  being the Universal baryon fraction), stellar feedback depends on the star formation rate  $\dot{M}_{\star}$  (or SFR) and AGN feedback depends on the BH accretion rate  $\dot{M}_{\text{BH}}$ . Thus, in this picture, galaxies can be fully described by the co-evolution among their stellar, BH, and dark matter contents, whose growths are intertwined. A direct consequence of this evolutionary scenario is that, at any redshift,  $M_{\text{h}}$ ,  $M_{\star}$ , and  $M_{\text{BH}}$  are expected to be related to each other. A careful characterization of the relations between these three quantities in nearby systems can give fundamental clues on the parameters that regulate galaxy evolution, and is the subject of this work.

Most studies in the literature have focused on the correlation between pairs of this leading trio. In particular, the relation between  $M_{\text{h}}$  and  $M_{\star}$  or, equivalently, between  $M_{\text{h}}$  and the galaxy global star formation efficiency  $f_{\star} \equiv M_{\star}/f_{\text{b}}M_{\text{h}}$ , has received a lot of attention from both the observational and the theoretical communities. From the theoretical side, this so-called stellar-to-halo mass relation (SHMR; for a recent review see Wechsler & Tinker 2018) is commonly probed via a semi-empirical technique known as abundance matching, which relates galaxies to haloes by matching the observed stellar mass function to the theoretical halo mass function obtained from cosmological  $N$ -body simulations, assuming that stellar mass increases

\* E-mail: antonino.marasco@inaf.it

monotonically with the mass of the host halo. Different abundance matching studies (e.g. Vale & Ostriker 2004; Behroozi, Conroy & Wechsler 2010; Moster, Naab & White 2013; Kravtsov, Vikhlinin & Meshcheryakov 2018) all point towards a scenario where  $f_*$  is maximal in galaxies with  $M_h \sim 10^{12} M_\odot$  (or  $M_* \sim 5 \times 10^{10} M_\odot$ ) and rapidly decreases at lower and higher  $M_h$ , which is traditionally interpreted as evidence for negative feedback from star formation in the low-mass regime and from AGN activity in the high-mass one. Observationally, the SHMR can be probed via different methods such as galaxy-galaxy weak lensing (Mandelbaum et al. 2006; Leauthaud et al. 2012), satellite or globular cluster kinematics (More et al. 2011; van den Bosch, Lange & Zentner 2019), internal galaxy dynamics (Cappellari et al. 2013; Read et al. 2017), or a combination of these (Dutton et al. 2010). Recent studies from Posti & Fall (2021) and Posti, Fraternali & Marasco (2019a) have found strong evidence for a difference in the SHMR of early- and late-type systems, with the former following the standard predictions from abundance matching models while the latter showing a monotonically increasing  $f_*$  as a function of mass, with no distinctive ‘peak’ in  $f_*$ . This discrepancy results in a substantially different  $f_*$  associated to the two galaxy types at  $M_* \sim 10^{11} M_\odot$  (that is, where most massive spirals are observed), suggesting the existence of different pathways for the stellar mass build-up in early- and late-type systems.

The existence of empirical correlations between the mass of the supermassive BH and the properties of the host galaxy bulge (like its mass  $M_{\text{bulge}}$  and velocity dispersion  $\sigma$ ) has been largely explored in the literature (for an in-depth review see Graham 2016) and is now well established (e.g. Magorrian et al. 1998; Marconi & Hunt 2003; Kormendy & Ho 2013; Saglia et al. 2016; de Nicola, Marconi & Longo 2019). The  $M_{\text{BH}}-\sigma$  relation, in particular, is among the tightest ones, with a vertical intrinsic scatter of  $\sim 0.3$  dex, which is often interpreted as evidence for co-evolution between the BH and the host bulge resulting from AGN feedback (King 2003; Somerville et al. 2008; King & Pounds 2015). Mergers can also play a role (Peng 2007; Jahnke & Macciò 2011), and there is evidence that the slope and normalization of the relation between  $M_{\text{BH}}$  and  $M_{\text{bulge}}$  (or  $\sigma$ ) depend on the galaxy structural parameters such as the bulge-to-total ratio and Sersic index (Graham & Scott 2013; Scott, Graham & Schombert 2013; Sahu, Graham & Davis 2019a, b). Spiral galaxies also exhibit a very tight (intrinsic scatter of  $\sim 0.3$  dex) correlation between  $M_{\text{BH}}$  and the spiral arm pitch angle (Seigar et al. 2008; Berrier et al. 2013; Davis, Graham & Seigar 2017), which is also supported by cosmological hydrodynamical simulations (Mutlu-Pakdil et al. 2018).

Surprisingly, however, the relation between  $M_{\text{BH}}$  and the total stellar mass of the host  $M_*$  has been explored much less in the literature and with somewhat contradictory results, ranging from being non-existent (Kormendy & Gebhardt 2001) to being as tight as the  $M_{\text{BH}}-M_{\text{bulge}}$  relation (Läscher et al. 2014). McConnell & Ma (2013) and Davis, Graham & Cameron (2018) gave more moderate views on the subject, showing the existence of a positive correlation between  $M_{\text{BH}}$  and  $M_*$  as expected from a co-evolution scenario (e.g. Bower et al. 2017, hereafter B17), although with a larger scatter with respect to the relations with the bulge properties.

Several theoretical models have suggested that the dynamically dominant component of a galaxy, i.e. its dark matter, should dictate the formation of BHs (e.g. Loeb & Rasio 1994; Haehnelt, Natarajan & Rees 1998; Booth & Schaye 2010, B17) as a direct consequence of the physics of gas accretion on to haloes. On the observational side, the pioneering works by Whitmore, Kirshner & Schechter (1979) and Whitmore & Kirshner (1981) highlighted the existence of a relation between the galaxy rotational velocity  $v_{\text{rot}}$ , traced by

H I kinematics, and the central velocity dispersion of the stellar component. However, it was Ferrarese (2002) who firstly interpreted this relation as evidence for a correlation between  $M_{\text{BH}}$  and  $M_h$ , since dark matter dominates the galaxy kinematics at large radii. The study of Ferrarese and later developments (e.g. Pizzella et al. 2005; Volonteri, Natarajan & Gültekin 2011) were criticized by Kormendy & Bender (2011), who showed that the correlation was apparent only in galaxies hosting a classical bulge, blaming the ‘rotation curve conspiracy’ (e.g. van Albada & Sancisi 1986) as a possible culprit for the observed trend. Sabra et al. (2015) used a sample of 53 galaxies of different morphological types with direct (dynamical) measurements of  $M_{\text{BH}}$  and only found evidence for an extremely weak correlation between  $v_{\text{rot}}$  and the BH mass. However, the sample of Sabra et al. (2015) was later expanded by Davis, Graham & Combes (2019b) and Smith et al. (2021), who concluded that a  $M_{\text{BH}}-v_{\text{rot}}$  relation for spiral galaxies exists, consistent with expectations from the joint  $M_{\text{BH}}-M_*$  and Tully & Fisher (1977) relations. Similar results were derived by Robinson et al. (2021) using a sample of 24 systems with  $M_{\text{BH}}$  measurements from reverberation mapping. One of the limitations of these studies is that they often make use of  $W_{50}$ , the line-width of the integrated velocity profile from H I or CO emission-line measurements, as a proxy for  $v_{\text{rot}}$ , which may lead to spurious results in cases where the rotation curve declines in the inner regions or the gas is not sufficiently extended in radius (e.g. Brook, Santos-Santos & Stinson 2016; Ponomareva et al. 2017).

These considerations indicate that, while several fragmented pieces of evidence for a co-evolution between stars, dark matter, and BHs in galaxies exist, steps need to be taken in order to build a more coherent observational picture, preparatory for constraining our theoretical understanding of galaxy evolution. The goal of this study is to provide important steps in this direction. On the one hand, we aim to clarify the relationship between  $M_{\text{BH}}$ ,  $M_h$ , and  $M_*$  (or rather, we prefer to focus on  $f_*$  instead of  $M_*$ ) from observational data. The main improvement with respect to previous works is that, from the large pool of systems with dynamical  $M_{\text{BH}}$  estimates, we select a suitable sub-sample with dynamical measurements of  $M_h$  coming, for the vast majority of objects, from either globular cluster kinematics (for galaxies of earlier Hubble types) or spatially resolved rotation curves from interferometric H I data (for galaxies of later Hubble types). Unlike studies that use H  $\alpha$  or CO data, which are limited to the inner regions of the galaxy, or H I line-width data from single-dish telescopes, which lack spatial resolution, the measurements used in this work allow to trace galaxy dynamics up to very large distances from the galaxy centers (typically  $\sim 50$  kpc) and are better suited to model the dark and luminous matter distribution in galaxies. In addition, we embed our observational results within a more general theoretical framework, showing that the observed relations are consistent with simple evolutionary models in  $\Lambda$ CDM where the stellar and BH mass built-up are regulated by the competition between positive and negative mechanisms discussed at the beginning of this section.

This paper is organized as follows. Our sample of nearby galaxies is described in Section 2 and the resulting scaling relations are presented in Section 3. Section 4 is dedicated to the building and the application of our model of galaxy evolution. The limitations of our model and the comparison with previous works are discussed in Section 5. Finally, Section 6 presents a summary and the conclusions of this study.

## 2 GALAXY SAMPLE

While several works have focused on the determination of galaxy BH, halo, and stellar masses separately, we are not aware of a

comprehensive study where these three quantities have been derived simultaneously in a homogeneous, self-consistent fashion. The main reasons for this are the very different physical scales associated to these masses, whose measurements requires very diverse data sets. Therefore, the galaxy sample used in this work is derived from a combination of different data sets, using a variety of approaches. We show that, in spite of such diversity, a coherent picture emerges. All halo masses presented in this study are computed within the radius where the mean halo density becomes equal to 200 times the critical density of the Universe, that is,  $M_h \equiv M_{200}^{\text{crit}}$ .

The first sample that we consider is that of Posti & Fall (2021, hereafter PF21), who used measurements of globular cluster radial velocities from the SLUGGS Survey (Brodie et al. 2014; Forbes et al. 2017) to perform a dynamical mass modeling of 25 nearby early-type galaxies. The  $M_*$  and  $M_h$  estimates of PF21 rely on the modeling of the phase-space distribution of globular clusters using a gravitational potential given by the sum of two spherical components, namely a Navarro-Frenk-White (NFW; Navarro, Frenk & White 1996) dark matter halo and a stellar bulge described by a Sersic (1968) profile. The SLUGGS data provide astrometric and spectroscopic measurements for several tens of clusters per object at distances up to  $\sim 12$  times the galaxy effective radii, effectively probing the large-scale galactic dynamics.  $3.6 \mu\text{m}$  images from *Spitzer Space Telescope* are used to constrain the distribution of the stellar components whose mass-to-light ratio is a free parameter of the model, along with the halo mass and concentration. We used the  $M_*$  and  $M_h$  provided by PF21 for a subsample of 18 of their systems that also have dynamical measurements of  $M_{\text{BH}}$  collected by Kormendy & Ho (2013) and Saglia et al. (2016). These are all based on stellar dynamics, with the exceptions of NGC 4526 (CO dynamics), NGC 4374, and NGC 4459 (ionized gas dynamics).

Next, we considered the sample of Terrazas et al. (2017), who have combined the data previously collected by Saglia et al. (2016) and van den Bosch (2016) to build a data set of 91 galaxies spanning different morphological types and with robust estimates for their  $M_{\text{BH}}$  from stellar, gas or maser dynamics. Stellar masses in Terrazas et al. (2017) are derived from extinction-corrected Ks-band photometry from 2MASS (Huchra et al. 2012). To determine the  $M_h$  of these objects, we have searched the literature for spatially resolved observations of large-scale kinematic tracers, preferably H I emission-line data but also H $\alpha$  or CO data. In cases where we judged the velocity field of such tracer to be regular enough so that a rotation curve could be determined reliably, we used  $v_{\text{flat}}$ , the rotational speed in the flat part of the rotation curve, as a proxy for  $M_h$ . The details of the  $v_{\text{flat}}$ -to- $M_h$  calibration are presented in Appendix A. When gas kinematics was not available, which is typically the case in earlier galaxy types, we used dynamical estimates based preferably on globular cluster radial velocities or, in the absence of these measurements, on modeling of the X-ray emitting halo gas, or on Schwarzschild models for the stellar component. Following this approach, we included a total of 30 galaxies from the Terrazas et al. (2017) sample. Finally, we complemented our data set with three additional objects from the recent sample of de Nicola et al. (2019), and four spiral galaxies from Kormendy & Ho (2013), following the same procedure described above to estimate the halo masses.

The main properties of the resulting sample of 55 galaxies are listed in Table 1, along with the references related to the  $M_{\text{BH}}$  and  $M_h$  measurements. The vast majority of galaxies in our sample have  $M_h$  determined with the rotation curve method (27, of which 21 from H I data, three from H $\alpha$ , one from CO and two from stellar kinematics) or from globular cluster dynamics (22). Schwarzschild models and the X-ray method are used only for four and two objects, respectively.

We stress that the  $M_h$  measurements used in this work have not been derived from observations alone, since none of the data extend to the halo virial radii. Instead, they are based on theoretical constraints on the properties of DM haloes in  $\Lambda$ CDM cosmological models, and in particular on the correlation between halo mass and concentration of Dutton & Macciò (2014), which our rotation curve method and the measurements of PF21 rely on. Aside from the 18 early types from PF21, where  $M_*$  is determined dynamically, we have homogenized the stellar mass measurements in our sample using a common  $M_*/L_K$  ratio of 0.6 (McGaugh & Schombert 2014). Other choices for  $M_*/L_K$  are possible, but have little impact on our results.

As most galaxies have  $M_h$  determined either from rotation curves or from globular cluster dynamics, it would be important to quantify how these two methods compare to each other. This is not trivial, given that globular clusters are more abundant in early-type galaxies where cold gas is typically scarce. In our sample, NGC 2974 is the only galaxy for which both measurements are available: using our equation (A1) with  $v_{\text{flat}} = 355 \pm 60 \text{ km s}^{-1}$  (from the H I study of Kim et al. 1988) gives  $\log_{10}(M_h/M_\odot) = 12.68 \pm 0.27$ , which perfectly agrees with the value found by PF21 and reported in Table 1,  $\log_{10}(M_h/M_\odot) = 12.71 \pm 0.30$ . This result, even if it is obtained for a single object, is reassuring and preparatory for the rest of the analysis.

### 3 OBSERVED SCALING RELATIONS

We now focus on the relations between  $f_*$ ,  $M_{\text{BH}}$ , and  $M_h$  for the systems in our sample. In Fig. 1, we show the distribution of our galaxies in the  $(M_{\text{BH}}, M_h)$  space (left-hand panel), in the  $(f_*, M_h)$  space (central panel), and in the  $(f_*, M_{\text{BH}})$  space (right-hand panel). It is evident that, in the mass range considered, each quantity appears to be related to the others. On average, the star formation efficiency decreases with increasing halo or BH masses, while  $M_h$  and  $M_{\text{BH}}$  are positively correlated with each other.

The correlation between  $M_{\text{BH}}$  and  $M_h$  does not come as a surprise, as it was firstly discovered by Ferrarese (2002). While we discuss this relation further in Section 5.1, we highlight here a couple of interesting features. First, the trend shown by the data at high  $M_h$  seems to break down around  $M_h$  of a few  $\times 10^{12} M_\odot$  (or  $M_{\text{BH}}$  of  $10^7 - 10^8 M_\odot$ ), steepening below this threshold mass. This feature may be simply produced by an increase in the scatter of the relation in the low  $M_h$  regime, possibly coupled with low-number statistics, but we will later show that a break in the  $M_{\text{BH}}-M_h$  relation arises ‘naturally’ in our galaxy evolution model as resulting from a change in the mode by which BHs accrete their gas. Secondly, the observed correlation is surprisingly tight. In Section 3.2 we show that, in our sample, the strength of the correlation between  $M_{\text{BH}}$  and  $M_h$  and its intrinsic scatter are comparable to those of a very well studied scaling law, the  $M_{\text{BH}}-\sigma$  relation.

The relation between  $f_*$  and  $M_{\text{halo}}$ , shown in the central panel of Fig. 1, is also not surprising. Galaxies are well known to follow a SHMR (e.g. Moster et al. 2013; Behroozi, Wechsler & Conroy 2013) according to which  $f_*$  peaks at the value of  $\sim 0.2$  for halo masses of  $\sim 10^{12} M_\odot$  and decreases rapidly at lower and higher  $M_h$ , possibly because star formation is made inefficient by stellar and AGN feedback, respectively. As the minimum  $M_h$  in our data is close to this peak value, we only sample the high-mass, descending portion of the SHMR. Interestingly, some low- $M_h$  galaxies in our sample have  $f_*$  compatible with 1, meaning that they have been able to convert all their (theoretically) available baryons into stars. The same result was found by Posti et al. (2019a) for a sample of high-

**Table 1.** Main properties for the sample of 55 nearby galaxies studied in this work.

Galaxy (1)	T-type (2)	$\log_{10}(M_{\text{BH}}/M_{\odot})$ (3)	$\log_{10}(M_{\text{h}}/M_{\odot})$ (4)	$\log_{10}(f_{\star})$ (5)	Ref. for $M_{\text{BH}}$ (6)	$M_{\text{h}}$ method (7)	Ref. for $M_{\text{h}}$ (8)
Milky Way	4.0	$6.63 \pm 0.04$	$12.11 \pm 0.10$	$-0.68 \pm 0.18$	KH13	GCs	Posti & Helmi (2019)
M 31	3.0	$8.15 \pm 0.16$	$12.08 \pm 0.30$	$-0.24 \pm 0.32$	KH13	RC (H I)	Corbelli et al. (2010)
M 66	3.1	$6.93 \pm 0.05$	$12.09 \pm 0.24$	$-0.62 \pm 0.28$	S16	RC (H $\alpha$ )	Chemin et al. (2003)
M 81	2.4	$7.81 \pm 0.13$	$12.01 \pm 0.24$	$-0.61 \pm 0.28$	S16	RC (H I)	de Blok et al. (2008)
Centaurus A	-2.1	$7.75 \pm 0.08$	$12.34 \pm 0.24$	$-0.81 \pm 0.28$	S16	RC (H I)	vanGorkom et al. (1990)
Circinus	3.3	$6.06 \pm 0.10$	$11.69 \pm 0.24$	$-0.86 \pm 0.28$	S16	RC (H I)	Jones et al. (1999)
NGC 307	-1.9	$8.60 \pm 0.06$	$12.02 \pm 0.24$	$-0.55 \pm 0.28$	S16	Schw	Erwin et al. (2018)
NGC 821	-4.8	$8.22 \pm 0.19$	$13.00 \pm 0.43$	$-1.27 \pm 0.46$	KH13	GCs	PF21
NGC 1023	-2.6	$7.62 \pm 0.04$	$12.98 \pm 0.65$	$-1.26 \pm 0.67$	KH13	GCs	PF21
NGC 1068	3.0	$6.92 \pm 0.24$	$12.18 \pm 0.24$	$-0.28 \pm 0.28$	S16	RC (H $\alpha$ )	Emsellem et al. (2006)
NGC 1097	3.3	$8.14 \pm 0.09$	$12.30 \pm 0.24$	$-0.66 \pm 0.28$	vdB16	RC (H I)	Ondrechen, van der Hulst & Hummel (1989)
NGC 1300	4.0	$7.88 \pm 0.30$	$12.13 \pm 0.24$	$-0.68 \pm 0.28$	KH13	RC (H I)	Lindblad et al. (1997)
NGC 1398	2.0	$8.03 \pm 0.08$	$12.54 \pm 0.24$	$-0.53 \pm 0.28$	S16	RC (H I)	Moore & Gottesman (1995)
NGC 1399	-4.6	$8.95 \pm 0.31$	$12.94 \pm 0.04$	$-1.01 \pm 0.16$	S16	GCs	Schuberth et al. (2010)
NGC 1407	-4.5	$9.67 \pm 0.05$	$13.70 \pm 0.31$	$-1.37 \pm 0.34$	S16	GCs	PF21
NGC 2273	0.9	$6.93 \pm 0.04$	$11.96 \pm 0.24$	$-0.60 \pm 0.28$	S16	RC (H I)	Noordermeer et al. (2007)
NGC 2748	4.0	$7.65 \pm 0.18$	$11.69 \pm 0.24$	$-0.63 \pm 0.28$	KH13	RC (H $\alpha$ )	Erroz-Ferrer et al. (2015)
NGC 2787	-1.0	$7.61 \pm 0.09$	$12.13 \pm 0.24$	$-1.48 \pm 0.28$	S16	RC (H I)	Shostak (1987)
NGC 2960	0.8	$7.03 \pm 0.05$	$12.43 \pm 0.24$	$-0.87 \pm 0.28$	S16	RC (H I)	Sun et al. (2013)
NGC 2974	-4.3	$8.23 \pm 0.08$	$12.71 \pm 0.30$	$-1.05 \pm 0.34$	S16	GCs	PF21
NGC 3079	6.4	$6.40 \pm 0.05$	$12.13 \pm 0.24$	$-0.82 \pm 0.28$	S16	RC (H I)	Sofue et al. (1999)
NGC 3115	-2.9	$8.95 \pm 0.08$	$13.01 \pm 0.62$	$-1.35 \pm 0.64$	KH13	GCs	PF21
NGC 3227	1.5	$7.32 \pm 0.23$	$12.26 \pm 0.24$	$-0.75 \pm 0.28$	S16	RC (H I)	Mundell et al. (1995)
NGC 3245	-2.1	$8.38 \pm 0.11$	$12.30 \pm 0.24$	$-0.97 \pm 0.28$	S16	RC (stars)	Zasov et al. (2012)
NGC 3377	-4.8	$8.25 \pm 0.23$	$12.22 \pm 0.34$	$-0.99 \pm 0.37$	KH13	GCs	PF21
NGC 3607	-3.2	$8.14 \pm 0.15$	$13.08 \pm 0.37$	$-0.96 \pm 0.40$	KH13	GCs	PF21
NGC 3608	-4.8	$8.67 \pm 0.09$	$13.15 \pm 0.55$	$-1.39 \pm 0.57$	KH13	GCs	PF21
NGC 3706	-3.2	$9.77 \pm 0.06$	$13.80 \pm 0.30$	$-1.81 \pm 0.34$	vdB16	Schw	Gültekin et al. (2014)
NGC 3783	1.4	$7.36 \pm 0.19$	$11.76 \pm 0.24$	$-0.15 \pm 0.28$	vdB16	RC (H I)	García-Barreto et al. (1999)
NGC 3923	-4.8	$9.45 \pm 0.12$	$13.44 \pm 0.15$	$-1.58 \pm 0.21$	S16	GCs	Norris et al. (2012)
NGC 3998	-2.2	$8.93 \pm 0.05$	$12.60 \pm 0.20$	$-1.42 \pm 0.25$	S16	Schw	Boardman et al. (2016)
NGC 4151	1.9	$7.81 \pm 0.08$	$11.80 \pm 0.24$	$-0.33 \pm 0.28$	S16	RC (H I)	Mundell et al. (1999)
NGC 4258	4.0	$7.58 \pm 0.03$	$12.02 \pm 0.24$	$-0.67 \pm 0.28$	S16	RC (H I)	Ponomareva, Verheijen & Bosma (2016)
NGC 4303	4.0	$6.51 \pm 0.74$	$11.76 \pm 0.24$	$-0.18 \pm 0.28$	vdB16	RC (H I)	Sofue et al. (1999)
NGC 4374	-4.4	$8.97 \pm 0.04$	$13.69 \pm 0.57$	$-1.45 \pm 0.59$	KH13	GCs	PF21
NGC 4388	2.8	$6.86 \pm 0.01$	$11.96 \pm 0.24$	$-0.91 \pm 0.28$	KH13	RC (H I) <sup>a</sup>	Woods, Madore & Fahlman (1990) Veilleux, Bland-Hawthorn & Cecil (1999)
NGC 4459	-1.6	$7.84 \pm 0.08$	$12.82 \pm 0.42$	$-1.11 \pm 0.45$	KH13	GCs	PF21
NGC 4472	-4.8	$9.40 \pm 0.04$	$13.98 \pm 0.30$	$-1.69 \pm 0.34$	S16	GCs	Côté et al. (2003)
NGC 4473	-4.7	$7.95 \pm 0.22$	$12.88 \pm 0.51$	$-1.19 \pm 0.53$	KH13	GCs	PF21
NGC 4486	-4.3	$9.81 \pm 0.06$	$13.75 \pm 0.24$	$-1.40 \pm 0.28$	KH13	GCs	PF21
NGC 4501	3.3	$7.30 \pm 0.08$	$12.37 \pm 0.24$	$-0.60 \pm 0.28$	S16	RC (CO)	Nehlig, Vollmer & Braine (2016)
NGC 4526	-1.9	$8.65 \pm 0.12$	$13.16 \pm 0.48$	$-1.17 \pm 0.50$	KH13	GCs	PF21
NGC 4564	-4.6	$7.94 \pm 0.12$	$12.88 \pm 0.78$	$-1.57 \pm 0.79$	KH13	GCs	PF21
NGC 4594	1.1	$8.82 \pm 0.04$	$12.73 \pm 0.24$	$-0.78 \pm 0.28$	S16	RC (H I)	Bajaja et al. (1984)
NGC 4649	-4.6	$9.67 \pm 0.10$	$13.76 \pm 0.43$	$-1.43 \pm 0.46$	KH13	GCs	PF21
NGC 4697	-4.5	$8.31 \pm 0.11$	$13.17 \pm 0.54$	$-1.29 \pm 0.56$	KH13	GCs	PF21
NGC 4736	2.3	$6.83 \pm 0.12$	$11.93 \pm 0.24$	$-0.76 \pm 0.28$	S16	RC (H I)	Speights et al. (2019)
NGC 4762	-1.8	$7.36 \pm 0.14$	$12.07 \pm 0.24$	$-0.52 \pm 0.28$	Krajnović et al. (2018)	RC (stars)	Fisher (1997)
NGC 4826	2.2	$6.19 \pm 0.13$	$11.69 \pm 0.24$	$-0.28 \pm 0.28$	S16	RC (H I)	Braun et al. (1994)
NGC 4945	6.1	$6.13 \pm 0.18$	$11.86 \pm 0.24$	$-0.70 \pm 0.28$	KH13	RC (H I)	Sofue et al. (1999)
NGC 5328	-4.7	$9.67 \pm 0.16$	$13.35 \pm 0.30$	$-1.31 \pm 0.34$	S16	X-ray	Trinchieri et al. (2012)
NGC 5846	-4.8	$9.04 \pm 0.05$	$13.85 \pm 0.45$	$-1.66 \pm 0.47$	S16	GCs	PF21
NGC 7052	-4.9	$8.60 \pm 0.23$	$12.91 \pm 0.30$	$-0.83 \pm 0.34$	S16	X-ray	Memola, Salucci & Babić (2011)
NGC 7457	-2.7	$6.95 \pm 0.26$	$12.02 \pm 0.47$	$-1.16 \pm 0.49$	KH13	GCs	PF21
NGC 7619	-4.8	$9.40 \pm 0.11$	$13.82 \pm 0.37$	$-1.80 \pm 0.40$	S16	Schw	Pu et al. (2010)

(1) Galaxy name; (2) morphological T-type from the HyperLEDA database; (3)–(5) BH mass, stellar mass, and star formation efficiency; (6) references for BH measurements: KH13-Kormendy & Ho (2013), S16-Saglia et al. (2016), and vdB16-van den Bosch (2016); (7) method used for  $M_{\text{h}}$  measurements: GCs-globular cluster dynamics, RC-rotation curve (using  $v_{\text{flat}}$  as described in the text), Schw-Schwarzschild model, X-ray- modeling of the X-ray-emitting circumgalactic gas; (8) references for  $M_{\text{h}}$  measurements. <sup>a</sup>  $v_{\text{flat}}$  comes from the mean of the two quoted studies.

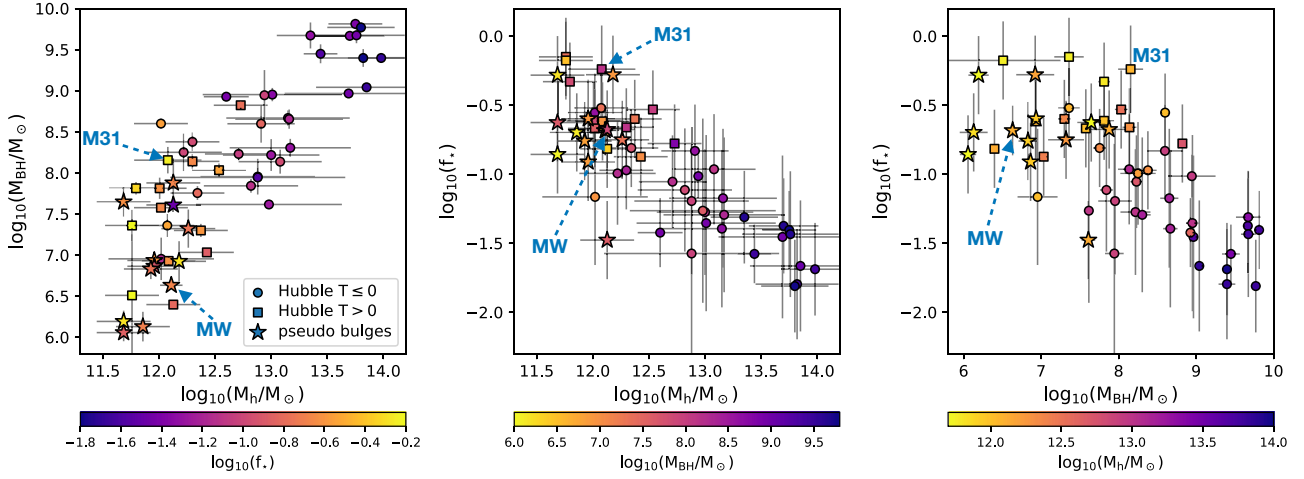


**Figure 1.**  $M_{\text{BH}}-M_{\text{h}}$  relation (leftmost panel)  $f_{\star}-M_{\text{h}}$  relation (central panel), and  $f_{\star}-M_{\text{BH}}$  relation (rightmost panel) in our galaxy sample. Markers in each panel are colour-coded according to the third dimension in the  $(M_{\text{h}}, M_{\text{BH}}, f_{\star})$  space. Circles (squares) are used for systems with Hubble morphological T-type  $\leq 0$  ( $> 0$ ), corresponding to early- (late-) galaxy types. Star markers are used for galaxies featuring pseudo-bulges in Kormendy & Ho (2013). As a reference, the locations of the Milky Way (MW) and M31 are shown.

mass spirals from the SPARC data set (Lelli, McGaugh & Schombert 2016).

The rightmost panel of Fig. 1 shows the anticorrelation between  $f_{\star}$  and  $M_{\text{BH}}$ . As noticed for the  $M_{\text{BH}}-M_{\text{h}}$  relation, also here the trend seems to change around  $M_{\text{BH}} \sim 10^{7.5} M_{\odot}$ : galaxies hosting lower-mass BHs have approximately constant  $f_{\star}$ , while at larger  $M_{\text{BH}}$  the star formation efficiency gets progressively reduced. As discussed before, the low-mass trend could also be due to an increase in the scatter, although here the break appears more evident. As this relation is less tight than that between  $f_{\star}$  and  $M_{\text{h}}$ , one may conclude that mass, and not BH feedback, is the main quenching driver in high-mass galaxies (e.g. Bundy et al. 2008; Peng et al. 2010b; Geha et al. 2012; Dubois et al. 2013). The results from our modeling (Section 4), however, suggest that this is not the case.

In Fig. 1, we have used different markers for galaxies of different morphology: circles show earlier galaxy types ( $T \leq 0$ ), squares show later galaxy types ( $T > 0$ ), while star markers highlight the spirals hosting pseudo-bulges as listed by Kormendy & Ho (2013). While early-type systems populate preferentially the high  $M_{\text{h}}$  regime and late-types appear only at lower  $M_{\text{h}}$ , the galaxy population as a whole seems to distribute along a well defined sequence in the  $M_{\text{BH}}-M_{\text{h}}-f_{\star}$  space. Discs hosting pseudo-bulges are no exception, as they do not occupy a preferential position in any of the three relations presented. We stress that the overlap between different galaxy types in the  $f_{\star}-M_{\text{h}}$  plane (central panel of Fig. 1) is not in tension with the results of PF21, who found distinct SHMR for early- and late-type systems: the split between morphological types becomes evident only in the  $f_{\star}-M_{\star}$  space (not shown here), due to the fact that the most massive early- and late-type galaxies, albeit having halo masses that differ by more than an order of magnitude, show only a factor 2–3 difference in  $M_{\star}$  (see fig. 3 in PF21).

The colour-coding used in Fig. 1 is useful to highlight another interesting feature of our data. The first and the third panel of Fig. 1 suggest that, at fixed  $M_{\text{BH}}$ , systems that have been more (less) efficient at forming stars are those that live in lower (higher) mass haloes. Conversely, no significant trend can be seen at fixed  $M_{\text{h}}$  (first and second panel). The features discussed can be better appreciated in Fig. 2. Here, we have determined empirically the mean trends of  $f_{\star}$

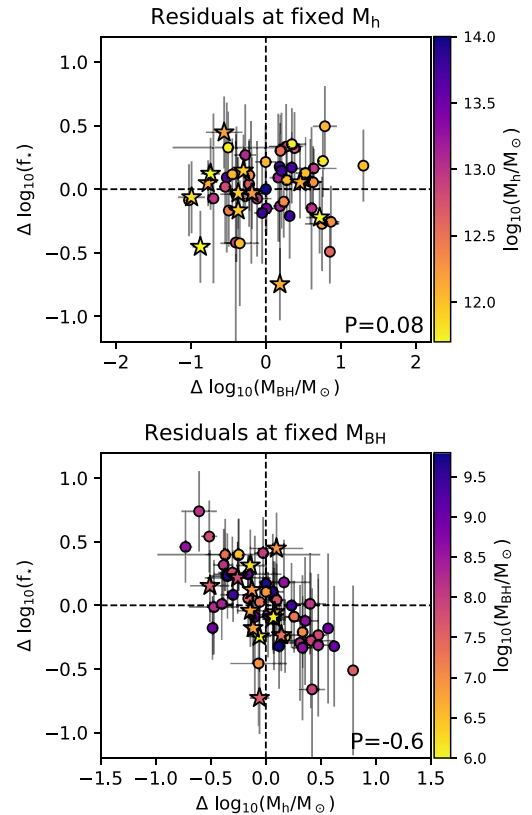


**Figure 2.** *Top panel:* residuals in the  $f_{\star}-M_{\text{h}}$  relation versus residuals in the  $M_{\text{BH}}-M_{\text{h}}$  relation for our galaxy sample. At fixed  $M_{\text{h}}$ , there is weak tendency for galaxies hosting heavier BHs to show larger  $f_{\star}$  (Pearson coefficient of 0.1). The colour palette shows the  $M_{\text{h}}$  of each galaxy. *Bottom panel:* residuals in the  $f_{\star}-M_{\text{BH}}$  relation versus those in the  $M_{\text{h}}-M_{\text{BH}}$  relation. At fixed  $M_{\text{BH}}$ , there is a strong evidence for galaxies living in lighter haloes to have larger  $f_{\star}$  (Pearson coefficient of  $-0.6$ ). The colour palette shows the  $M_{\text{BH}}$  of each galaxy. The markers used in both panels are the same as in Fig. 1.

and  $M_{\text{BH}}$  as a function of  $M_{\text{h}}$ , and plotted the residuals with respect to these trends against each other in the top panel of Fig. 2. The clear lack of an anticorrelation between these residuals is surprising, as one might expect that galaxies hosting larger BHs are also those where AGN feedback, and therefore star formation quenching, is more effective. In contrast, there is instead weak evidence for a positive correlation (Pearson coefficient of 0.1). Similarly, the residuals with respect to the mean  $f_{\star}-M_{\text{BH}}$  and  $M_{\text{h}}-M_{\text{BH}}$  relations are compared in the bottom panel of Fig. 2. The anticorrelation between  $f_{\star}$  and  $M_{\text{h}}$  at fixed BH mass becomes now very evident (Pearson coefficient of  $-0.6$ ). In Section 4.2, we show that uncorrelated scatter in the parameters of our evolution model can explain the trends shown in Fig. 2 remarkably well. In particular, system-to-system variability in BH feedback efficiency is a viable explanation for the observed anticorrelation between  $f_{\star}$  and  $M_{\text{h}}$  at fixed  $M_{\text{BH}}$ .

### 3.1 The 3D $M_{\text{BH}}-M_{\text{h}}-f_{\star}$ relation

We now analyse the distribution of our galaxy sample in the 3D ( $f_{\star}$ ,  $M_{\text{BH}}$ ,  $M_{\text{h}}$ ) space. The eigenvalues of the covariance matrix associated to our data are approximately in a 26:3:1 ratio. The presence of a substantially larger eigenvalue indicates that there is a clear tendency for the data to distribute along a unique direction in the 3D space, given by the associated eigenvector. This is a simple geometrical confirmation of the fact that  $M_{\text{BH}}$ ,  $M_{\text{h}}$ , and  $f_{\star}$  are all related to each other, as previously discussed. It also suggests that, in the mass range studied here, measuring either  $M_{\text{BH}}$ ,  $M_{\star}$ , or  $M_{\text{h}}$  in a galaxy suffices to determine the other two quantities, with good approximation.

The 3:1 ratio of the two lower eigenvalues indicate that a (marginally) more refined representation for our data is given by a plane in the 3D space considered. We used the LTSFIT PYTHON package from Cappellari et al. (2013) to fit our data with the following parametric form:

$$\log(f_{\star}) = a \log_{10} \left( \frac{M_{\text{h}}}{M_{\odot}} \right) + b \log_{10} \left( \frac{M_{\text{BH}}}{M_{\odot}} \right) + c. \quad (1)$$

The code uses a least-squares fitting algorithm which allows for intrinsic scatter and errors in all coordinates. The best-fitting solution is found for  $a = -0.77 \pm 0.15$ ,  $b = 0.13 \pm 0.09$ ,  $c = 7.70 \pm 0.05$ , and is consistent with no intrinsic scatter. The parameters found are indicative of the same trends discussed above, i.e.  $f_{\star}$  depends strongly on  $M_{\text{h}}$  at a fixed  $M_{\text{BH}}$ , but very weakly (or not at all) on  $M_{\text{BH}}$  at a fixed  $M_{\text{h}}$ . The best-fitting parameters of equation (1) remain within the quoted uncertainties if we fit only the data with  $M_{\text{h}} > 10^{12} M_{\odot}$  (that is, we exclude the data points below the break).

Fig. 3 offers two representative 3D views of the data, along with the best-fitting plane and the theoretical model that we build in Section 4. The 3D views clearly highlight how the data distribute preferentially along a 1D sequence, although a plane can capture the distribution of their scatter. We stress, though, that the plane described by equation (1) is valid exclusively in the range of masses spanned by the data, and in particular it will not hold at  $M_{\text{h}} < 5 \times 10^{11} M_{\odot}$ , a regime where  $f_{\star}$  is known to decrease, rather than increase as equation (1) would suggest.

### 3.2 Relating $M_{\text{BH}}$ to the properties of the stellar component

The importance of characterizing the relations between  $M_{\text{BH}}$  and other observable galaxy properties is twofold. On the one hand, these relations provide fundamental clues to constrain the physics of BH growth and to clarify the role of AGN feedback in galaxy evolution. On the other hand, the existence of tight scaling relations

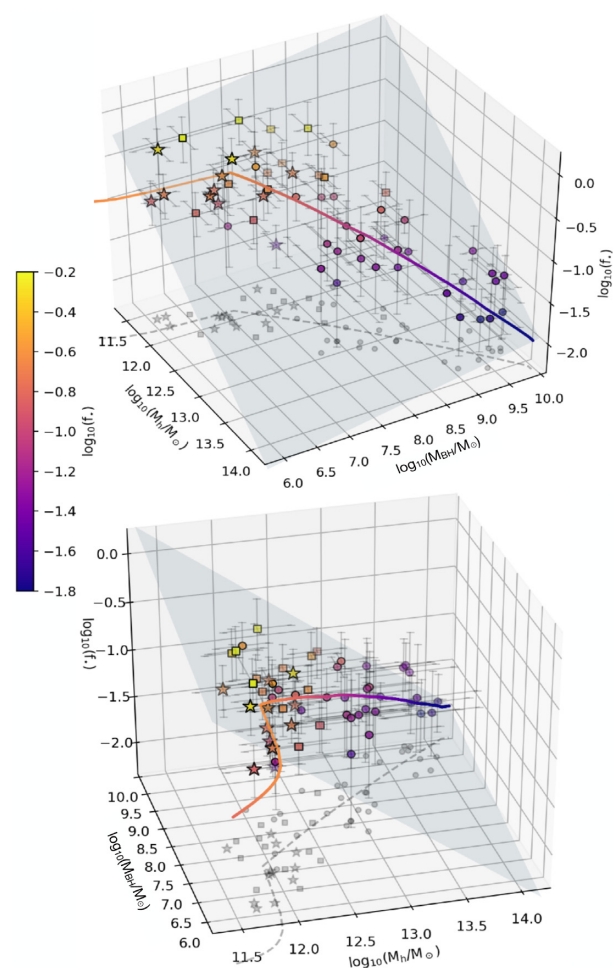


**Figure 3.** Two different 3D views for the distribution of our galaxy sample in the ( $M_{\text{h}}$ ,  $M_{\text{BH}}$ ,  $f_{\star}$ ) space. The markers used in both panels are the same as in Fig. 1. The best-fitting plane from equation (1) is shown in dark grey. The 3D curve passing through the data shows the fiducial theoretical model from Section 4. To better enhance the 3D perspective, galaxies are colour-coded by their  $f_{\star}$  and 2D projections on the ( $M_{\text{h}}$ ,  $M_{\text{BH}}$ ) plane are shown.

offer convenient ways to determine the BH masses using more easily observable quantities as proxies. While the primary focus of this study is the relation between  $M_{\text{BH}}$  and global galaxy properties such as  $M_{\text{h}}$  and  $f_{\star}$ , in this section, we briefly discuss how BH masses relate to some of the properties of the stellar component in our galaxy sample.

Fig. 4 shows the relations between  $M_{\text{BH}}$  and four different stellar properties: the total stellar mass  $M_{\star}$ , the stellar disc mass  $M_{\text{disc}}$ , the stellar bulge mass  $M_{\text{bulge}}$ , and the mean stellar velocity dispersion within the effective radius  $\sigma_e$ . The  $M_{\text{BH}}-M_{\text{h}}$  relation, already discussed in Section 3, is also shown as a reference. The  $\sigma_e$  measurements adopted here are from de Nicola et al. (2019) and Kormendy & Ho (2013), while bulge fractions are mostly based on the 2D-decompositions of  $3.6 \mu\text{m}$  images from the the Spitzer Survey of Stellar Structure in Galaxies (Sheth et al. 2010) via the GALFIT package (Peng et al. 2002, 2010a) or, when these were not available, on the kinematic decomposition reported in Fall & Romanowsky (2018). Each panel in Fig. 4 reports the Spearman (S) and Pearson (P) correlation coefficients of the quantity pair analysed, and the best-fitting parameters of linear (in log-space) regression determined with LTSFIT, including the intrinsic scatter in the vertical and perpendicular

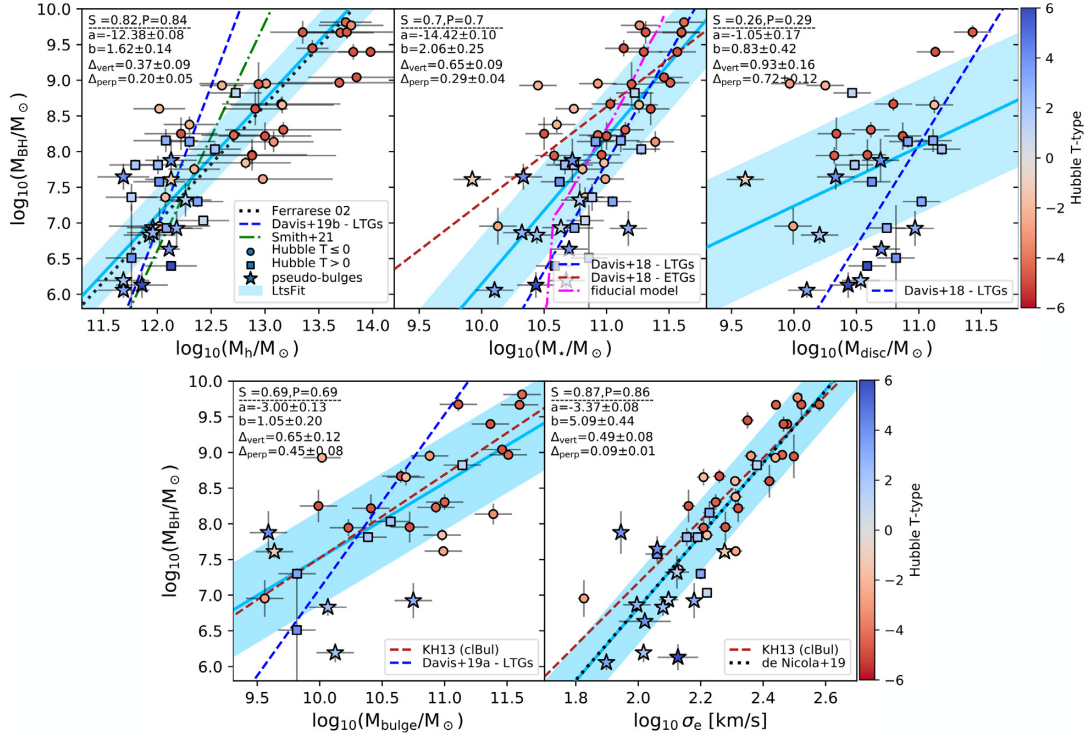


**Figure 4.** Relations between  $M_{\text{BH}}$  and other galaxy properties in our sample: halo mass  $M_{\text{h}}$  (top-left panel), stellar mass  $M_{\star}$  (top-middle panel), stellar disc mass  $M_{\text{disc}}$  (top-right panel), stellar bulge mass  $M_{\text{bulge}}$  (bottom-left panel), and mean stellar velocity dispersion within the effective radius  $\sigma_e$  (bottom-right panel). Symbols are the same as in Fig. 1, colour-coded by the Hubble morphological type of each galaxy. In the top-left corner of all panels, we list the Spearman (S) and Pearson (P) correlation coefficients of the data, followed by the intercept (a), slope (b), vertical, and perpendicular intrinsic scatter ( $\Delta_{\text{vert}}$  and  $\Delta_{\text{perp}}$ ) of the best-fitting linear regression determined with LTSFIT (Cappellari et al. 2013). The best-fitting relation is shown as a light-blue solid line, with the filled region corresponding to  $\pm\Delta_{\text{vert}}$  around it. Dotted and dashed lines in the various panels show some of the scaling relations previously reported in the literature and are discussed in Section 5.1.

directions,  $\Delta_{\text{vert}}$  and  $\Delta_{\text{perp}}$ . Galaxies in Fig. 4 are colour coded by their Hubble morphological T-type, taken from the HyperLEDA database. Fig. 4 also shows a representative selection of the best-fitting relations previously determined in the literature, which will be discussed in more detail in Section 5.1.

The correlation coefficients that we find confirm the widely accepted scenario according to which (i) the stellar property that best correlates with  $M_{\text{BH}}$  is  $\sigma_e$ ; (ii) bulges correlates with  $M_{\text{BH}}$  much better than discs. However, in our sample, the strength of the correlation between  $M_{\text{BH}}$  and  $M_{\text{h}}$  (correlation coefficients of  $\sim 0.83$ ) is comparable to that between  $M_{\text{BH}}$  and  $\sigma_e$  ( $\sim 0.86$ ). We also find a lower  $\Delta_{\text{vert}}$  in the  $M_{\text{BH}}-M_{\text{h}}$  relation than in the  $M_{\text{BH}}-\sigma_e$  relation, although this is probably due to the large uncertainties associated with our  $M_{\text{h}}$  estimates. All considered, our results indicate that both  $\sigma_e$  and  $M_{\text{h}}$  seems to provide a similar accuracy when used as proxies for the BH mass, which is quite remarkable given the completely different scales involved. We stress, though, that the perpendicular intrinsic scatter  $\Delta_{\text{perp}}$  of the  $M_{\text{BH}}-\sigma_e$  is about half that of the  $M_{\text{BH}}-M_{\text{h}}$ , indicating that the former is more ‘fundamental’ than the latter. The relation between  $\sigma_e$  and  $M_{\text{h}}$  (not presented here) shows a trend similar to that between  $M_{\text{BH}}$  and  $M_{\text{h}}$ , with a hint of a break visible around  $\sigma_e$  of  $130-160 \text{ km s}^{-1}$ . As discussed by PF21, a correlation between these two quantities is expected as resulting from the combination of the SHMR, which links  $M_{\text{h}}$  to  $M_{\star}$ , and the Faber & Jackson (1976) and Tully & Fisher (1977) relations, which relate  $M_{\text{star}}$  to a characteristic velocity of the stellar component (that is,  $\sigma_e$  for early-galaxy types).

Another interesting feature shown by the data is that the  $M_{\text{BH}}-M_{\text{bulge}}$  relation shows similar strength and intrinsic scatter as

the  $M_{\text{BH}}-M_{\star}$  relation. This means that, in our sample, the bulge mass and the total stellar mass are equally good proxies for  $M_{\text{BH}}$ , which is a puzzling result considering the poor correlation between  $M_{\text{BH}}$  and  $M_{\text{disc}}$ . The top-right panel of Fig. 4 may give a clue to the solution of this puzzle, indicating that earlier and later galaxy types follow somewhat parallel sequences in the  $M_{\text{BH}}-M_{\text{disc}}$  plane. This results in an overall poor correlation between BH and disc masses, but when bulges are included in the total  $M_{\star}$  budget the sequence of early-types approaches the other one, increasing the overall correlation strength. A similar result was also found by Davis et al. (2018), who stressed the importance of distinguishing between early- and late-galaxy types in the study of the  $M_{\text{BH}}-M_{\star}$  (see also Section 5.1). We note, however, that relative to a unbiased, volume-limited sample, massive discs are over-represented (shallower mass function) in our sample while massive spheroids are under-represented (steeper mass function). This limitation, together with the fact that bulge/disc fraction measurements are available only for 70 per cent (39/55) of it, restrain us from investigating these features further in this work.

Finally, we stress that the correlation coefficients and best-fitting parameters determined in this section do not vary significantly when galaxies hosting pseudo-bulges are removed from the analysis. The main difference is visible in the  $M_{\text{BH}}-M_{\text{h}}$  relation, whose slope decreases when these low-mass systems are removed. However, this would be readily explained if the intrinsic shape of the  $M_{\text{BH}}-M_{\text{h}}$  relation was not a simple power-law, but its slope increases at lower masses as we suggest in the section below. Similarly, moderate ( $\sim 30$  per cent) variations in the mass-to-light ratios of discs and bulges have little impact on the results presented in this section.

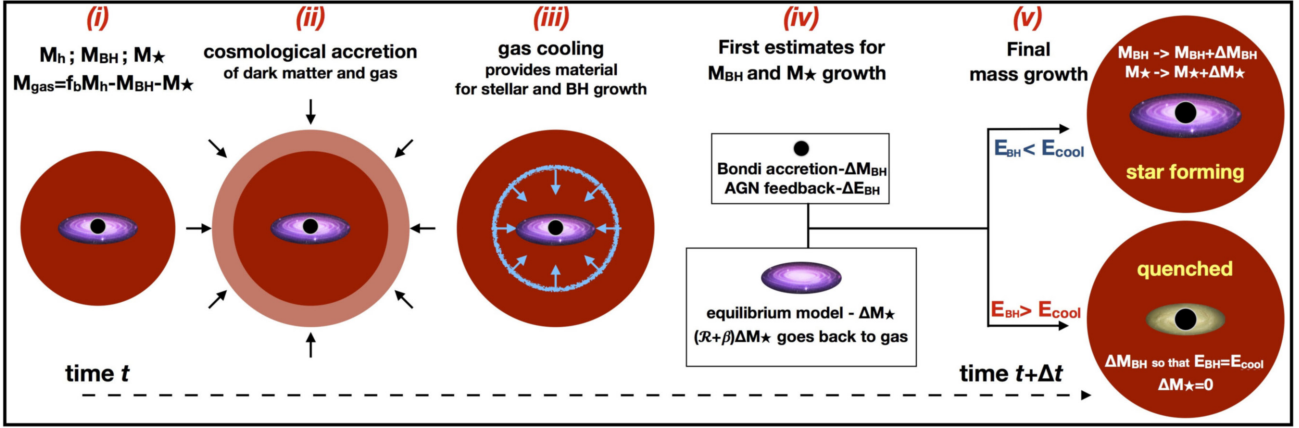


**Figure 5.** Sketch showing the sequence of physical processes regulating the mass build-up in our galaxy evolution framework within a time interval  $[t, t + \Delta t]$ . (i) At a time  $t$ , the galaxy is fully described by its  $M_h$ ,  $M_{BH}$ , and  $M_*$ . Its gas content  $M_{gas}$  (ISM+CGM) is such that the total baryonic mass is  $f_b M_h$ . The gas temperature is set to the halo virial temperature. (ii) Dark matter and gas accrete on to the halo at a cosmological rate given by equation (B1). (iii) A fraction of  $M_{gas}$  cools, instantaneously providing fuel for star formation and BH accretion. The cooling mass depends on the variation of the gas mass enclosed within the cooling radius ( $r_{cool}$ , equation B2) in the time interval considered. (iv) A first estimate for the mass accreting on to the BH,  $\Delta M_{BH}$ , is computed via equations (B7) and (B8). A first estimate for the mass of the newly formed stars  $\Delta M_*$  is computed via the equilibrium model, equation (B3). The energy injected by the AGN feedback into the gas reservoir is increased by an amount  $\Delta E_{BH}$  given by equation (B9). (v)  $E_{BH}$  is compared to the gas gravitational binding energy within the cooling radius,  $E_{cool}$  (equation B10). If  $E_{BH} < E_{cool}$ , the BH mass is increased by  $\Delta M_{BH}$  and the stellar mass by  $\Delta M_*$ , otherwise  $\Delta M_{BH}$  is reduced so that  $E_{BH} = E_{cool}$  and  $\Delta M_*$  is set to zero.

#### 4 A SIMPLE GALAXY EVOLUTION MODEL

In this section, we investigate the physical origin of the trends presented in Section 3 using a simple equilibrium model for galaxy evolution in the  $\Lambda$ CDM framework.<sup>1</sup> Our model is largely inspired by the work of B17 and is based on a commonly accepted framework where galaxy haloes smoothly accrete dark matter and gas at a cosmological rate, having their stellar and BH build-up regulated both by the cooling of the available gas reservoir and by stellar/AGN feedback. We provide a full description of our model in Appendix B, while below we give a brief overview – sufficiently detailed to follow the rest of this study – of its main ingredients.

The model follows the evolution of BH, stellar, and dark matter masses of a galaxy given some initial conditions, namely the initial ‘seed’ masses  $M_{BH, seed}$  and  $M_{h, seed}$ , and the seeding cosmological time  $t_{seed}$ . At each time-step, the mass growths of the various components are determined via the sequence of physical processes illustrated in Fig. 5. These include standard recipes for cosmological accretion of dark matter and gas on to haloes, gas radiative cooling, star formation, BH accretion, and simplified treatments for stellar and AGN feedback. The galactic gas reservoir, intended as the sum of interstellar and circumgalactic media (ISM and CGM), is described as a single component following an equation of state with  $\gamma = 4/3$  (as in B17), with a temperature equal to the halo virial temperature, a mass given by  $f_b M_h - M_* - M_{BH}$ , and a pristine metallicity (chemical enrichment is not treated in our model, but a case with a higher metallicity is discussed in Section 4.2). At each time-step, the gas cooling rate is balanced by the rates at which stars form, the BH grows and gas is returned to the initial reservoir because of stellar mass losses and feedback (‘equilibrium’ model). In our implementation, feedback from star formation has two effects: it

drives galaxy-scale outflows which instantly return gas to the initial reservoir, with a mass-loading  $\beta$  equal to  $(M_h/M_{crit})^{-\alpha}$  ( $M_{crit}$  and  $\alpha$  being free parameters), and it acts as a regulator of the gas density close to the BH, significantly reducing its accretion rate for large  $\beta$  (e.g. Hopkins et al. 2021). AGN feedback is treated as a continuous accumulation of energy deposited by the BH on to the gas reservoir at a rate  $\propto \epsilon_f \dot{M}_{BH}$ ,  $\epsilon_f$  being the BH feedback efficiency, another free parameter. The total energy released by the BH,  $E_{BH}$ , must not exceed the gravitational binding energy of the cooling gas,  $E_{cool}$ : at time-steps when this occurs, the BH accretion rate is reduced so that the condition above is satisfied, and star formation is manually turned off. This form of ‘preventative’ AGN feedback is the only quenching channel that we provide in our galaxy evolution framework. The main parameters regulating our model are summarized in Table 2, while the caption of Fig. 5 points to the relevant equations defined in Appendix B.

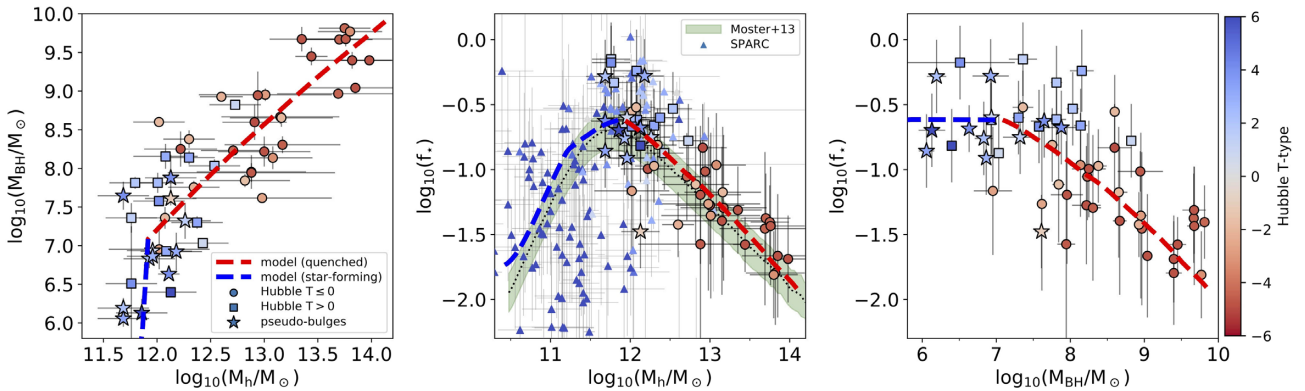
We stress that the final goal of this modeling exercise is to offer a simple but cosmologically motivated interpretation for the observed scaling relations between BH, stellar and halo masses presented in Figs 1 and 3. While we acknowledge that  $M_{BH}$  correlates more strongly with  $M_{bulge}$  than with  $M_{disc}$  (Section 3.2), here we do not offer separate treatments for the growth via smooth accretion or via episodic mergers and treat the galaxy stellar component as a whole. This simplifies our approach significantly, bypassing the need for prescriptions regulating the formation of bulges which would introduce additional complexity to the model. Clearly, the use of such simplification implies that we will not get physical insights on the co-evolution between bulges and BHs. For instance, we cannot distinguish a scenario where the  $M_{BH}-M_{bulge}$  relation results from the physics of stellar and AGN feedback, which separately produce  $M_{BH} \propto \sigma^4$  and  $M_{bulge} \propto \sigma^4$  scalings (Power et al. 2011; King & Nealon 2021), from a scenario where the  $M_{BH}-M_{bulge}$  arises statistically from the hierarchical merging of galaxies with initially uncorrelated  $M_{BH}$  and  $M_{bulge}$  (Peng 2007; Jahnke & Macciò 2011). We leave the answer to this topic to more dedicated theoretical studies, though our simple model still provides useful insights once compared to the presented correlations between  $M_{BH}$  and global galaxy properties.

<sup>1</sup>We assume a Planck Collaboration XVI (2014) cosmology ( $\Omega_{m,0} = 0.315$ ,  $H_0 = 67.3 \text{ km s}^{-1} \text{ Mpc}^{-1}$ ), in particular  $f_b \equiv \Omega_b/\Omega_c = 0.188$ .

<sup>2</sup>Hence, the total mass of baryons within the halo is always equal to  $f_b M_h$ , which implies that the gas accreted on to the halo never leaves the system.

**Table 2.** Main parameters of our theoretical model of galaxy evolution. The values listed for the free parameters are those of our fiducial model discussed in Section 4.1.

Parameter	Description	Value	Status
$t_{\text{seed, min}}$	Earliest seed injection time	0.3 Gyr ( $z = 13.9$ )	Fixed
$t_{\text{seed, max}}$	Latest seed injection time	4.0 Gyr ( $z = 1.62$ )	Fixed
$M_{\text{h, seed}}$	Seed halo mass	$10^{10} M_{\odot}$	Fixed
$M_{\star, \text{seed}}$	Seed stellar mass	$10^3 \times M_{\text{BH, seed}}$	Fixed
$Z_{\text{gas}}$	Gas metallicity	pristine	Fixed
$\mathcal{R}$	Recycled gas fraction due to stellar mass losses	0.3	Fixed
$M_{\text{BH, seed}}$	Seed black hole mass	$5 \times 10^4 M_{\odot}$	Free
$\rho_{\text{BH, 0}}$	Normalization of the gas density near the BH, equation (B8)	$0.35 \text{ cm}^{-3}$	Free
$\epsilon_f$	BH feedback efficiency, equation (B9)	$1.0 \times 10^{-2}$	Free
$M_{\text{crit, 0}}$	Present-day critical halo mass, equation (B5)	$2.5 \times 10^{11} M_{\odot}$	Free
$\alpha$	Slope of the mass-loading due to stellar feedback, equation (B4)	1.7	Free

**Figure 6.** Fiducial model at  $z = 0$  (thick dashed curves) versus observational data from this work. Markers are the same as in Fig. 1, but colour-coded by the Hubble morphological type of each galaxy. *Left-hand panel:*  $M_{\text{BH}}$  versus  $M_{\text{h}}$ . *Central panel:*  $f_{\star}$  versus  $M_{\text{h}}$ , triangles are measurements from Posti et al. (2019a) using SPARC spirals (Lelli et al. 2016), the green-shaded region shows the abundance matching prediction from Moster et al. (2013). *Right-hand panel:*  $f_{\star}$  versus  $M_{\text{BH}}$ . In all panels, the blue- (red-) dashed curve show model galaxies that are star forming (quenched) at  $z = 0$ .

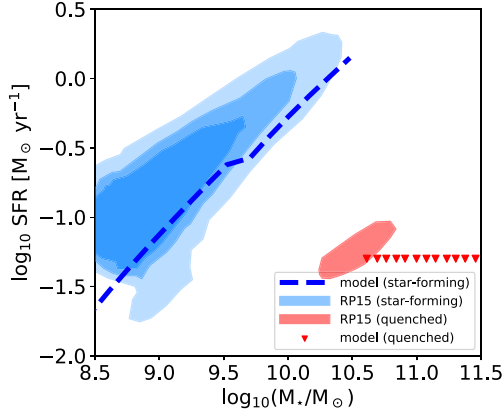
#### 4.1 A fiducial model

Table 2 shows a summary of the main parameters of our equilibrium model. By experimenting with different parameter values, we have found a ‘fiducial’ set which produces a model in excellent agreement with our data at  $z = 0$ . The fiducial parameter set is reported in the bottom portion of Table 2 and the comparison with the data is presented in Fig. 6. Clearly, our model predicts a  $M_{\text{BH}}-M_{\text{h}}-f_{\star}$  relation (dashed lines in Fig. 6) which passes right through the data. In particular, the model predicts a break in the relations at  $M_{\text{BH}} \simeq 10^7 M_{\odot}$  which is visible in our data as well, as discussed in Section 3. In the central panel of Fig. 6, we also show the SHMR determined by Moster et al. (2013) from abundance matching prediction (green-shaded region), and the dynamical measurements of Posti et al. (2019a) for the spirals from the SPARC data set (Lelli et al. 2016), which allows us to extend the dynamical range of the  $f_{\star}-M_{\text{h}}$  plot down to lower masses. However, measurements for  $M_{\text{BH}}$  in the SPARC sample are not available. Our model performs very well along the entire mass range. Interestingly, the measurements from SPARC indicate that the scatter in the SHMR increases at lower  $M_{\text{h}}$ , a point which we will return to in Section 4.2. A 3D view of the fiducial model was already offered in Fig. 3.

While our model seems to correctly predict the relations between stellar, halo, and BH masses, which are quantities integrated over cosmic time, one may question its performance when it comes to more ‘instantaneous’ properties, like the SFRs of present-day

galaxies. In our model, the SFR of a system is abruptly shut down when the BH energy output becomes equal to the binding energy of gas within the halo cooling radius. We show below that this happens earlier in more massive haloes, while in less massive galaxies this may only occur at  $t > t_{\text{Hubble}}$ . This produces a segregation between low-mass systems that are normally star forming at  $z = 0$ , and high-mass galaxies that are quenched. Fig. 7 shows the relation between the SFR, averaged over the latest 100 Myr of evolution, and the stellar mass of  $z = 0$  systems in our fiducial model, and compares it with the approximate observed distribution from SDSS measurements by Renzini & Peng (2015). Our model correctly reproduces the slope ( $\sim 1$ ) of the main sequence of star formation (e.g. Noeske et al. 2007; Popesso et al. 2019), albeit with a slightly lower normalization (by  $\sim 0.2$  dex), as well as the approximate  $M_{\star}$  at which quenched galaxies begin to dominate the SFR- $M_{\star}$  distribution (that is, around  $10^{10.5} M_{\odot}$ ). Clearly, the transition between these two regimes is supposed to be gradual, whereas in our simplified treatment of BH feedback it is abrupt. We discuss this further in Section 5. Going back to Fig. 6, we have used blue and red dashed-lines to show the star-forming and quenched galaxy populations, respectively. In our fiducial model, at  $z = 0$  the transition occurs at  $M_{\text{h}} \simeq 10^{12} M_{\odot}$ , so that most of the systems studied in this work are supposed to be quenched. While this may not be the case for individual galaxies, our results hold for the galaxy population as a whole.

Further insights on the evolutionary scenarios predicted by our fiducial model are provided by Fig. 8, where we show the dark



**Figure 7.** SFR averaged over the last 100 Myr versus  $M_*$  at  $z = 0$ . The blue dashed line and the red triangles show galaxies from our fiducial model that are star forming or quenched, respectively. The SFR of quenched system is set to an arbitrarily low value. The blue (red) shaded region shows the approximate distribution for star-forming (quenched) systems in SDSS from Renzini & Peng (2015).

matter, stellar, and BH mass build-up as a function of  $z$  for systems of different present-day  $M_h$ . By construction, the halo growth (panel a in Fig. 8) proceeds undisturbed at all  $z$  and for all systems. The BH growth (panel c), instead, is more interesting. At high  $z$ , the BH accretion proceeds slowly, both because seeds are still small and because supernova-driven outflows are very efficient at lowering the central gas density. As stellar feedback becomes less efficient, this early phase is then followed by a very rapid growth, which ends abruptly only when  $E_{\text{BH}} \simeq E_{\text{cool}}$ . Then, the accretion proceeds at a more gradual pace in a self-regulating mode driven by the continuous balance between  $E_{\text{BH}}$  and  $E_{\text{cool}}$ . This balance defines univocally the slope of the  $M_{\text{BH}}-M_h$  relation for  $M_h \gtrsim 10^{12} M_\odot$ , whose excellent agreement with the data is one of the main success of our simple theoretical model. The  $z$  at which the transition to the self-regulating accretion mode occurs is a function of the galaxy mass: high-mass systems enter the self-regulating phase earlier, whereas galaxies with  $M_h(z=0) \lesssim 10^{12} M_\odot$  (corresponding to  $M_{\text{BH}}(z=0) \lesssim 10^7 M_\odot$ ) are still in the rapidly accreting mode. This agrees well with the picture of antihierarchical growth of BHs emerging from the study of AGN luminosity functions (e.g. fig. 8 in Marconi et al. 2004), and produces the break in the scaling relations visible around BH masses of  $10^7 - 10^8 M_\odot$  (see Fig. 1). Also, this transition between the rapidly accreting phase and the self-regulating phase signals the end of the stellar mass build up (panel b). As the transition occurs earlier in more massive haloes, the redshift at which quenching occurs increases for increasing  $M_*(z=0)$ , which is again in agreement with the picture

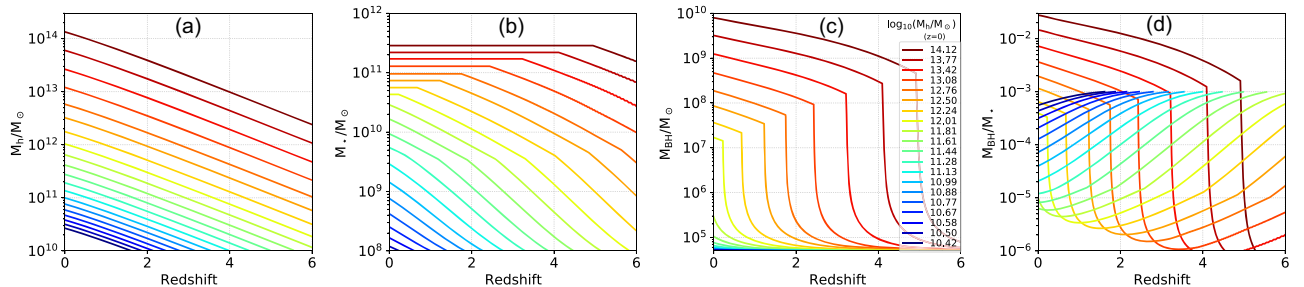


**Figure 8.** Dark matter (a), stellar (b), and BH (c) mass build-up as a function of redshift in our fiducial model, colour-coded by the halo mass reached at  $z = 0$ . Panel (d) shows the evolution of the BH-to-stellar mass ratio.

of antihierarchical growth of galaxies (or ‘downsizing’; e.g. Cowie et al. 1996; Eyles et al. 2005; Fontanot et al. 2009). However, in our model, the BHs of quenched galaxies still accrete gas because  $M_h$  and  $E_{\text{cool}}$  keep growing with time, requiring increasingly higher  $E_{\text{BH}}$  for the balancing. Thus the BH-to-stellar mass ratio increases with time in most massive haloes (panel d), which seems to be at odds with predictions from other theoretical models (e.g. Lamastra et al. 2010) and with observational data (e.g. Merloni et al. 2010), although observational bias at high- $z$  may play an important role (Lauer et al. 2007). We discuss further the limitations of our modeling approach in Section 5.3.

The reader may have noticed that we have avoided any statistical approach to optimize the model parameters to the observed data. In fact, the fiducial values reported in Table 2 are only indicative, and we do not exclude that a better match could be obtained by tuning the parameters further or even using very different parameter values. The spirit of our approach is to offer a proof of concept that a simple equilibrium model in  $\Lambda$ CDM framework is well suited for describing many of the observed trends, rather than offering precise estimates for some parameter values.

## 4.2 Interpreting the observed scatter

One of the most interesting features of our data lies in their scatter, and in particular in the correlations between the residuals shown in Fig. 2. In this section, we explore the possibility that such correlations arise ‘naturally’ in our model because of random fluctuations in the model parameters.

As a first step, it is instructive to assess how the  $M_{\text{BH}}-M_h-f_*$  relation predicted at  $z = 0$  responds to variations in the single model parameters. This is shown in Fig. 9, where we compare our fiducial model with a series of other realizations obtained by varying one by one the various parameters while keeping the others fixed to their fiducial values. This exercise reveals a number of interesting features. First, the high-mass slope of the  $M_{\text{BH}}-M_h$  relation remains the same in all our experiments, indicating that it is a strong prediction of the self-regulated accretion mechanism described above. Its normalization instead depends entirely on  $\epsilon_f$  (panel c in Fig. 9): as expected, higher BH masses are reached for lower feedback efficiencies, and vice versa. Surprisingly,  $\epsilon_f$  has no impact on the SHMR. As we discuss in Section 5.3, this is due to the primary role of BH in processing the gas accreted from the halo and can be seen as a consequence of our oversimplified treatment of star formation processes. In practice,  $\epsilon_f$  regulates the fraction of  $\dot{M}_{\text{cool}}$  that feeds the BH in the self-regulating phase, but (by construction) the fraction that does not accrete on to the BH does not form stars either, leaving no impact on the SHMR. The role of  $M_{\text{BH, seed}}$  and  $n_{\text{BH}, 0}$  is to set the BH

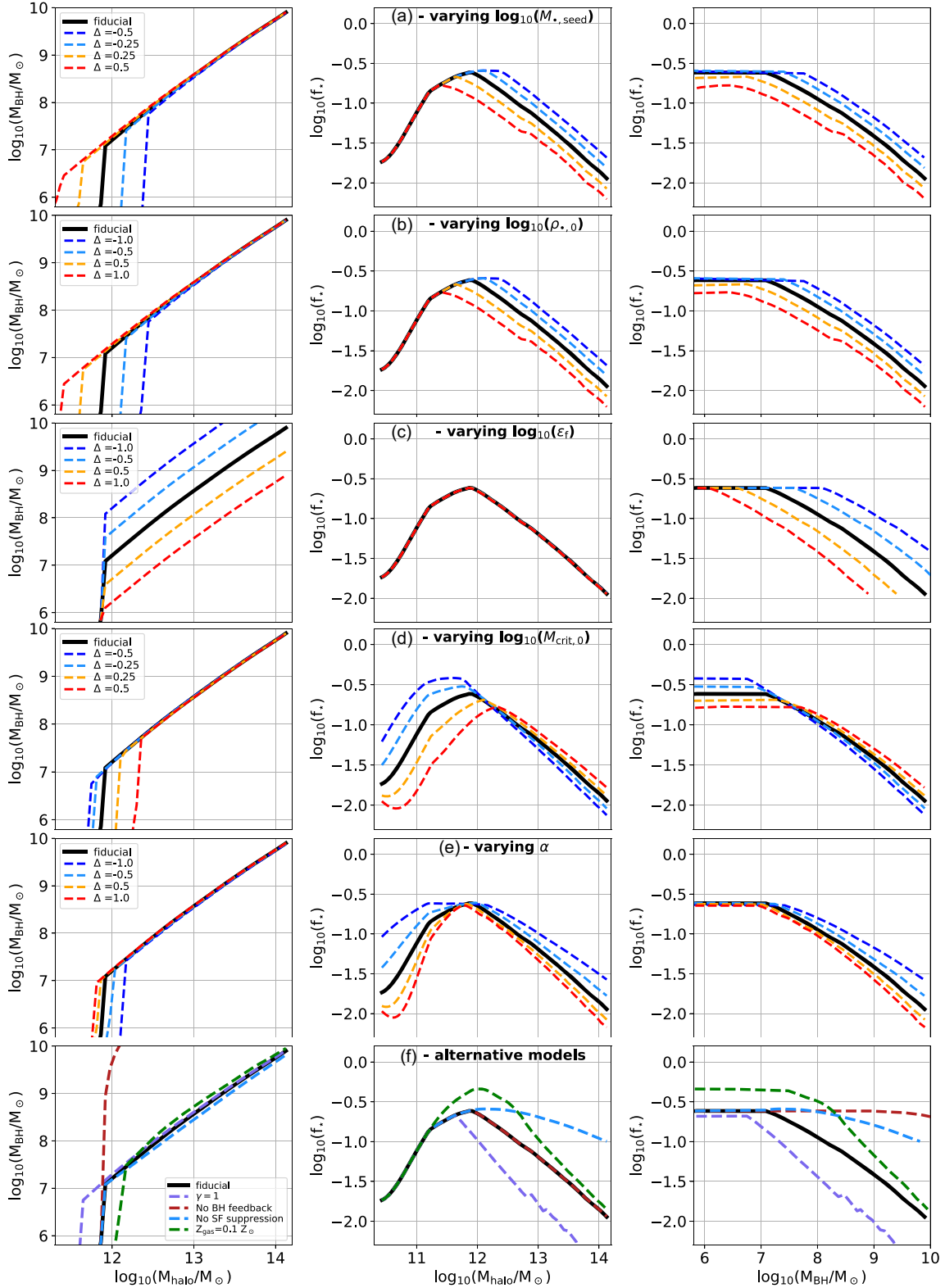


**Figure 9.** Comparison between our fiducial model (black solid curves in all panels) and models obtained using different parameter values (coloured dashed curves). Panels-sets (a)–(e) show the effects of varying a single parameter while keeping the others fixed to their fiducial values. The variations  $\Delta$  indicated in each panel are in dex, with the exception of those for  $\alpha$  which are in linear units. Panel-set (f) explores alternative models where (i) the gas that accretes on to the BH is described by an isothermal equation of state (purple); (ii) the metallicity of the gas reservoir is set to  $0.1 Z_{\odot}$  (green); (iii) BH feedback is suppressed (red); (iv) BH feedback is made incapable of quenching star formation (blue).

accretion rate via equation (B6) during the phase that precedes the self-regulating mode, effectively shortening or extending the self-regulating sequence in the  $M_{\text{BH}}-M_{\text{h}}$  plane and affecting the post-peak part of the SHMR (panels a and b). We note that  $M_{\text{BH, seed}}$  and  $n_{\text{BH, 0}}$  are completely degenerate in the mass range considered, which is another reason for considering the values quoted in Table 2 as indicative only. Finally, the parameters regulating the stellar feedback efficiency,  $\alpha$  and  $M_{\text{crit, 0}}$ , play a major role in setting the slope of the SHMR at all masses and its normalization at low masses, respectively (panels e and d). Thus, in our models, stellar feedback participates in regulating the star formation efficiency at all masses (via  $\alpha$ ), and not only in the low- $M_{\text{h}}$  regime.

The panel-set (f) in Fig. 9 shows the effect of altering some of the main assumptions of the model, and deserves a more in-depth discussion. The coefficient of the equation of state for the gas accreting on to the BH has an influence on the slope of the SHMR in the high-mass regime: using  $\gamma = 1$  in equation (B7; isothermal gas) leads to a steeper slope (purple dashed curves) that is not compatible with the data and that cannot be easily changed by varying the other parameters of the model. Removing completely the BH feedback from our fiducial model (that is, assuming  $\epsilon_{\text{f}} = 0$ ) leads to overmassive BHs in all galaxies, as shown by the red dashed curves in the panels. Allowing the BH growth to self-regulate without suppressing also the star formation in systems with  $E_{\text{BH}} > E_{\text{cool}}$  leads to a much flatter high-mass slope for the SHMR (blue dashed curves), which means that star formation quenching driven by BH feedback is an important ingredient in our model. Finally, the green dashed curves show the effect of increasing the gas metallicity from pristine to  $0.1 Z_{\odot}$ . This promotes gas cooling and effectively enhances the star formation efficiency, increasing the maximum  $f_{\star}$  achievable without changing the peak mass. This would give a better agreement the high- $f_{\star}$  values measured for the most massive spirals of the SPARC sample (Posti et al. 2019a), and for some of the systems in our sample as well. While modeling the metallicity evolution of the galactic gas reservoir goes beyond the purpose of the present study, we stress that the peak  $f_{\star}$  reached by our fiducial model may well be underestimated given the pristine composition assumed for the gas accreted at all redshift.

The above experiments offer an interpretation of the scatter seen in the data. From panel-set (c) in Fig. 9, it is clear that a scatter in  $\epsilon_{\text{f}}$  produces an anticorrelation between  $f_{\star}$  and  $M_{\text{h}}$  at a fixed  $M_{\text{BH}}$ . This happens because, as  $\epsilon_{\text{f}}$  scatters from lower to higher values, galaxies hosting BH of similar mass occupy more massive haloes (that is, generated from earlier seeds), which necessarily correspond to lower values of  $f_{\star}$ , as the SHMR is not sensitive to  $\epsilon_{\text{f}}$ . Fluctuations in  $M_{\text{crit, 0}}$ , instead, offer a way to obtain both a positive correlation between  $f_{\star}$  and  $M_{\text{BH}}$  at a fixed  $M_{\text{h}}$  (but only in the low- $M_{\text{h}}$  regime), and a higher scatter in the low- $M_{\text{h}}$  part of the SHMR.

These considerations can be better visualized in Fig. 10, which shows a stochastic realization of our fiducial model obtained by introducing Gaussian fluctuations, with standard deviation of 0.4, in  $\log(\epsilon_{\text{f}})$ ,  $\log(M_{\text{crit, 0}}/M_{\odot})$  and  $\alpha$ . The colour-coding follows that of Fig. 1 and helps one recognize, within the model, the same features seen in the data and discussed in Section 3. By fitting equation (1) to this synthetic data set, after excluding systems with  $M_{\text{h}} < 5 \times 10^{11} M_{\odot}$  or  $M_{\text{BH}} < 10^6 M_{\odot}$  (grey circles in Fig. 1) which do not have a counterpart in the observed sample, we find  $a = -0.68$ ,  $b = 0.05$ , and  $c = 7.21$ . These values are in excellent agreement with those found for our observed data set in Section 3.1. In Fig. 11, we show the relations between the residuals calculated at fixed  $M_{\text{h}}$  and  $M_{\text{BH}}$  in our scattered model, computed following the same procedure used for the data in Fig. 2. The comparison between Figs 2 and

10 shows remarkable similarities between the data and the model (similar Pearson coefficients). Including also fluctuations in  $M_{\text{BH, seed}}$  and  $\rho_{\text{BH, 0}}$  does not alter the trends seen in the residual, although the agreement with the data worsens. Although qualitative, these considerations indicate that a simple, uncorrelated scatter in the model parameters may well explain the features observed the data residuals.

Once again, the experiments presented in this section must be considered as a proof of concept that the data can be well reproduced by models like the one presented in this work. The physical origin for the scatter in the model parameters is a matter of great relevance, but its investigation goes beyond the purpose of this study.

## 5 DISCUSSION

### 5.1 Comparison with other works

The positive, tight correlation between  $M_{\text{h}}$  and  $M_{\text{BH}}$  was first noticed by Ferrarese (2002) as a consequence of the correlation between rotational velocity and central velocity dispersion in galaxies (originally discovered by Whitmore et al. 1979), the former being a proxy for  $M_{\text{h}}$  and the latter for  $M_{\text{BH}}$ . Later on, Bandara, Crampton & Simard (2009) provided a more direct evidence for a correlation between  $M_{\text{BH}}$  and the total dynamical mass of the galaxy  $M_{\text{dyn}}$  by focusing on a sample of early-type systems for which  $M_{\text{dyn}}$  were determined via gravitational lensing models. A similar  $M_{\text{BH}}-M_{\text{dyn}}$  relation was derived by Krumpe et al. (2015) by studying the X-ray luminosity dependence on the clustering strength of low- $z$  AGNs. Interestingly, the original  $M_{\text{BH}}-M_{\text{h}}$  relation determined by Ferrarese (2002), shown as a black dotted line in the top-left panel of Fig. 4, is in a remarkably good agreement with our data, in spite of the different methods used to determine BH masses and the different  $v_{\text{flat}} - M_{\text{h}}$  calibration adopted, and with the results of Bandara et al. (2009) and Krumpe et al. (2015).

The findings of Ferrarese (2002) were very surprising as they indicated that dark matter alone could engineer the BH growth without passing through the complex baryonic physics associated with BH accretion. Kormendy & Bender (2011) and later Kormendy & Ho (2013) have argued against such conclusion, pointing out that the  $M_{\text{BH}}-M_{\text{h}}$  relation holds only for classical bulges and is not followed by spirals hosting pseudo-bulges or by bulgeless discs, which would suggest that that it comes as a byproduct of the co-evolution between spheroids – arguably formed by mergers and therefore strictly related to the accretion history of haloes – and BHs. In our study, we have shown that all galaxies participate in the same  $M_{\text{BH}}-M_{\text{h}}$  relation (left-hand panel in Fig. 1). This seems to be the case also for the 12 spirals that host pseudo-bulges, although our statistics are heavily affected by the limited mass range where these are present within our sample ( $11.5 < \log_{10}(M_{\text{h}}/M_{\odot}) < 12.3$ ). The  $M_{\text{BH}}-M_{\text{h}}$  relation, however, appears to change slope at  $M_{\text{h}}$  of a few  $\times 10^{12} M_{\odot}$  (or  $M_{\text{BH}}$  of  $10^7 - 10^8 M_{\odot}$ ), which suggests an origin from different competing mechanisms. In the theoretical framework of Section 4, these competing mechanisms are the stellar feedback at low  $M_{\text{h}}$  and the AGN feedback at high  $M_{\text{h}}$ . At  $M_{\text{h}} \lesssim 10^{12} M_{\odot}$ , feedback from stars regulate the density of cold gas near the BH, and since in our model the stellar feedback efficiency depends on  $M_{\text{h}}$  via equation (B4), a  $M_{\text{BH}}-M_{\text{h}}$  relation follows. At higher  $M_{\text{h}}$ , the BH regulates its own growth as its accretion rate is limited by the balance between the AGN feedback energy and the cold gas gravitational binding energy. Since the gas cooling rates and the binding energy both depend on  $M_{\text{h}}$ , another  $M_{\text{BH}}-M_{\text{h}}$  relation follows, albeit with a different slope. Ultimately, a relation between  $M_{\text{BH}}$ ,  $M_{\star}$ , and  $M_{\text{h}}$  must be expected in any galaxy evolution framework where the material

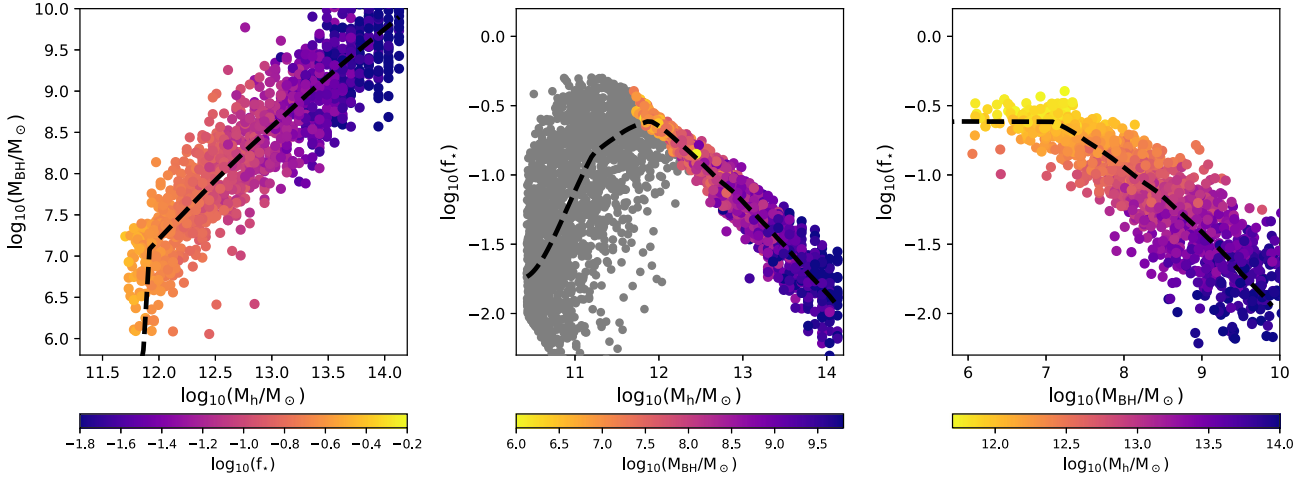


**Figure 10.** Stochastic realization of our fiducial model at  $z = 0$  including a Gaussian scatter, with a standard deviation of 0.4, in  $\log(\epsilon_f)$ ,  $\log(M_{\text{crit},0}/M_\odot)$  and  $\alpha$ . The colour-coding adopted is the same of Fig. 1. Grey circles are used for systems with  $M_h < 5 \times 10^{11} M_\odot$  or  $M_{\text{BH}} < 10^6 M_\odot$ , which do not have a counterpart in the observed sample. The black dashed curves show the model without scatter.

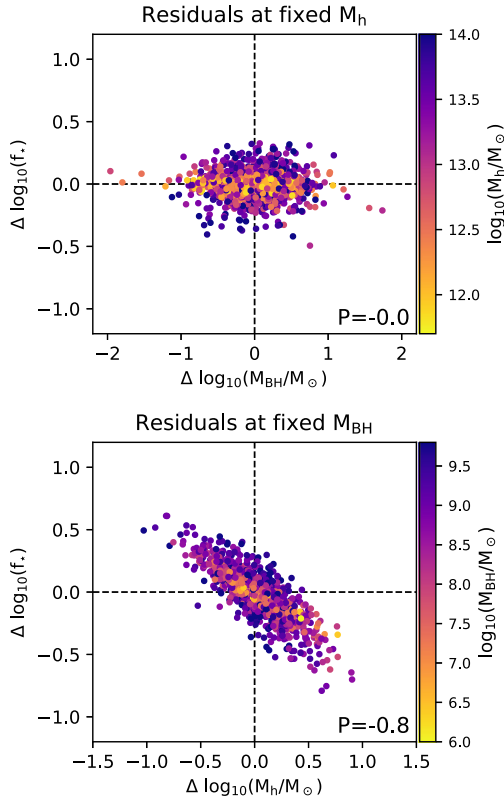


**Figure 11.** Residual correlation plot, analogous to that of Fig. 2, for a stochastic realization of our fiducial model at  $z = 0$  including a Gaussian scatter of 0.4 in  $\log_{10}(\epsilon_f)$ ,  $\log_{10}(M_{\text{crit},0}/M_\odot)$  and  $\alpha$ . Only systems with  $M_h > 5 \times 10^{11} M_\odot$  and  $M_{\text{BH}} > 10^6 M_\odot$  are shown.

used for the stellar and BH build-up is provided by the cooling of the halo gas reservoir.

de Nicola et al. (2019) used a sample of 83 galaxies with different morphologies and high-quality  $M_{\text{BH}}$  measurements to investigate the correlations between  $M_{\text{BH}}$  and the host galaxy properties. Not surprisingly, our data are in perfect agreement with the best-fitting  $M_{\text{BH}}-\sigma_e$  relation of de Nicola et al. (2019; dotted black line in the

bottom-right panel of Fig. 4) as the majority of our  $\sigma_e$  measurements come from their study. More noticeably, they also agree well with the relation reported by Kormendy & Ho (2013) for classical bulges (red-dashed line in the same panel), especially in the high-mass regime. Interestingly, galaxies with  $\sigma_e < 150\text{--}200 \text{ km s}^{-1}$  show a characteristic deviation from the best-fitting  $M_{\text{BH}}-\sigma_e$  line that closely mimics that observed in the  $M_{\text{BH}}-M_h$  plane. This is only partially visible in our Fig. 4, but is much more evident in the larger sample of de Nicola et al. (2019, see the top panel of their fig. 2). This points towards the existence of a tight correlation between  $M_h$  and  $\sigma_e$ .

Davis et al. (2019b) studied a sample of 44 spiral galaxies with dynamical measurements of  $M_{\text{BH}}$ , using the line-width of the integrated velocity profile (from HI or H $\alpha$  data) as a proxy for  $v_{\text{flat}}$ , which is then converted to  $M_h$  using the calibration from Katz et al. (2019). A similar study was more recently done by Smith et al. (2021) using both spatially resolved and unresolved CO observations, and including early-type systems too. The  $M_{\text{BH}}-M_h$  relations resulting from these two studies are shown in the top-left panel<sup>3</sup> of Fig. 4, and are consistent with our data only in the low-mass regime. However, there are differences between our study and those of Davis et al. (2019b) and Smith et al. (2021) in terms of both methods and goals. As for methods, we have used a more complete galaxy sample spanning different morphological types, and relied on separate techniques to determine  $M_h$  depending on the galaxy morphology: spatially resolved rotation curves in late-types, which we carefully selected from the literature, and globular cluster dynamics in early-types, mostly coming from the work of PF21. This allowed us to see features in the data, namely the break in the relation, that were not apparent in the samples of other studies. As for goals, rather than focusing on characterizing the  $M_{\text{BH}}-M_h$  relation in order to use one quantity as a proxy for the other, we made the attempt to encapsulate our results in a theoretical framework, with the purpose of understanding the physical origin for the observed trends.

In a series of recent works, Davis et al. (2018), Davis, Graham & Cameron (2019a), and Davis et al. (2019b) have focused on

<sup>3</sup>Here, we used the  $v_{\text{flat}}\text{-to-}M_h$  calibration from equation (A1) and, for the results of Smith et al. (2021), assumed  $v_{\text{flat}} \simeq W_{50}/2\sin(i)$ ,  $i$  being the galaxy inclination.

characterizing the scaling relations between  $M_{\text{BH}}$  and the host galaxy properties in late-type systems, which until then had received little attention in the literature. The scaling relations resulting from their studies, shown as blue dashed lines in the various panels of Fig. 4, are in good agreement with our data when only late-type (Hubble  $T > 0$ ) galaxies are considered, but are in tension with the full sample which includes many early-type objects. This discrepancy is particularly severe in the  $M_{\text{BH}}-M_{\text{bulge}}$  plane (bottom-left panel of Fig. 4), where our data indicate a much shallower slope, virtually identical to that found by Kormendy & Ho (2013) for classical bulges (red dashed line in the same panel), with respect to the scaling found by Davis et al. (2019a). Davis et al. (2018) compared their  $M_{\text{BH}}-M_{\star}$  relation determined in 40 spirals with that derived using 21 early-type galaxies from the sample of Savorgnan et al. (2016), finding significant differences in the slope and normalization. The two relations reported by Davis et al. (2018) are shown in the top-middle panel of Fig. 4, and indeed appear to better describe separately the two galaxy types. Our fiducial model, shown as a magenta dot-dashed line in the same panel, is ignorant of galaxy morphology and predicts a unique relation that passes mostly in between the two sequences of Davis et al. (2018).

Our theoretical model is largely inspired by the work of B17, who however focused almost entirely on how BH growth in haloes is related to the development of the ‘red’ and ‘blue’ galaxy sequences in the present-day Universe. B17 clearly showed the peculiar shape of the  $M_{\text{BH}}-M_{\text{h}}$  relation, which we found to be in excellent agreement with the data, and suggested the use of equilibrium models as possible improvements for their approach. We have followed their suggestion here so that  $f_{\star}$  can be predicted from within the same framework that models the evolution of dark matter haloes and BHs.

While we model the cooling of gas reservoir in haloes, it must be expected that BH fueling is primarily governed by physical processes occurring at sub-kpc scales rather than by large-scale cosmological infall. Recently, Hopkins et al. (2021) presented a model in which the fraction of gas available for BH fueling is regulated by feedback from star formation occurring in the central ( $R < 1$  kpc) galaxy regions. At these radii, the time-scales over which stellar feedback operates are longer than the dynamical time-scales: this prevents the onset of an ‘equilibrium’ phase where the thickness of the gas layer smoothly adjusts to the turbulence injected by stellar feedback (e.g. Marasco et al. 2015; Bacchini et al. 2020), producing instead a galaxy-scale outflow with an efficiency that depends on the central surface density. This model implies that BH masses trace the host galaxy properties above a critical surface brightness (typical of bulges), and correctly predicts the slope and normalization of the  $M_{\text{BH}}-\sigma$  and the  $M_{\text{BH}}-M_{\text{bulge}}$  relations. Our model is not tailored to reproduce ‘local’ galaxy properties but it includes a conceptually similar prescription, inherited from B17: the density of gas near the BH scales as the inverse of the mass loading factor  $\beta$  (equation B8). Since  $\beta$  depends on  $M_{\text{h}}$  (equation B4), galaxies with  $M_{\text{h}} < M_{\text{crit}}$  feature a severe deficit in their central gas density and their BHs grow slowly. Conversely, stellar feedback has virtually no impact on the BH growth at higher  $M_{\text{h}}$ , which is regulated instead by the balance between  $E_{\text{BH}}$  and  $E_{\text{cool}}$  (unlike the model of Hopkins et al. 2021, which does not consider AGN feedback).

We stress that more refined semi-analytical models than the one presented here are available in the literature (e.g. Croton et al. 2006; Somerville et al. 2008; Guo et al. 2013; Henriques et al. 2015; Behroozi et al. 2019). These approaches include several ingredients such as mergers, environmental effects, different modes of AGN-driven feedback, and are designed to capture the evolution of chemical abundances and angular momentum of galaxies in addition

to the quantities studied here. However, none of these works have focused specifically on the  $M_{\text{BH}} - M_{\text{h}} - f_{\star}$  relation, most likely because of the lack of high-quality data available at the time of the writing. We expect that the data set built in this work (Table 1) will be useful for theorists to constrain future models of galaxy evolution.

Cosmological hydrodynamical simulations in the  $\Lambda$ CDM framework such as Illustris (Vogelsberger et al. 2014) predict relations between  $M_{\star}$ ,  $M_{\text{BH}}$ ,  $M_{\text{h}}$ , and spiral arm pitch angle in qualitative agreement with the observations (Mutlu-Pakdil et al. 2018). A more quantitative comparison with between these predictions and the data set built in the present work would provide useful constraints to galaxy evolution models.

## 5.2 Considerations on galaxy morphology

It is well known that galaxy colour and morphology are strongly correlated: while the galaxy population transits from the ‘blue cloud’ of star-forming systems to the ‘red sequence’ of quenched ones, it also undergoes a structural transformation from a preferentially disc-dominated to a more spheroid-dominated morphology (Roberts & Haynes 1994; Baldry et al. 2004; Muzzin et al. 2013; Kelvin et al. 2014). In this section, we explore the morphology distribution of our sample and interpret it in the framework of our model.

We turn our attention to the colour-coding used in Fig. 6, which indicates the morphological Hubble T-type. The morphology distribution is strongly bi-modal in  $M_{\text{h}}$ , with late- (early-) type systems systematically occupying haloes with masses below (above)  $\sim 3 \times 10^{12} M_{\odot}$ . This corresponds to a similarly sudden transition around  $f_{\star}$  of 0.15–0.2. The same bimodal behaviour was already noticed by PF21. The transition as a function of  $M_{\text{BH}}$  appears instead to be more gradual and occurs at BH masses between  $10^7 M_{\odot}$  and  $3 \times 10^8 M_{\odot}$ , roughly where the break in the BH scaling relations appears.

We already touched upon the different scalings followed by the different morphological types in Section 5.1. Considering earlier and later types separately in Fig. 6, one may argue that the two categories obey different scaling laws, as the separation in the  $M_{\text{BH}}-M_{\text{h}}$  space and, above all, in the  $f_{\star}-M_{\text{BH}}$  space is visible. However, our theoretical model predicts a unique relation in the  $M_{\text{BH}}-M_{\text{h}}-f_{\star}$  space. While information on morphology (or angular momentum) are not specifically encoded within our model, one may question the existence of a single evolutionary sequence valid for all galaxy types.

Fully addressing the question above goes beyond the purpose of this study, but a qualitative argument comes from the fact that, at a fixed  $M_{\text{BH}}$ , galaxies with higher  $f_{\star}$  do not only live in lighter haloes (see Section 3 and Fig. 2) but also have later morphological types (rightmost panel of Fig. 6). In our theoretical framework, lighter haloes at  $z = 0$  are always associated to later seeds which, due to their relatively short lifespan, had a lower probability of experiencing major mergers that could induce a morphological transformation (e.g. Hopkins et al. 2010; Martin et al. 2018). Hence our model, which reproduces the correlations shown in Fig. 2 (Section 4.2), can also qualitatively explain the trends with the morphological type. We stress that, within this framework, the relation between galaxy quenching and morphological transformation is indirect: quenching is caused by BH growth and feedback, which is more significant in more massive haloes; more massive haloes are produced by earlier seeds, which have a higher probability of experiencing morphological transformations induced by major mergers. In a more realistic scenario, however, it is likely that galaxy mergers have an impact on the growth of the central BH. For instance, mergers can funnel gas towards the central regions of the galaxy, thus promoting

BH growth and triggering AGN feedback (e.g. Hopkins et al. 2006). Also, variations in the angular momentum of a galaxy have an impact on the stability of its disc and can possibly affect the evolution of  $f_*$  as suggested by Romeo, Agertz & Renaud (2020). In general, the BH accretion rate may increase if the overall angular momentum of the galaxy gets reduced (which may be the case after a major merger). These considerations suggest that the relationship between galaxy structure and quenching are more complex than suggested by our simple framework.

### 5.3 Limitations of our model

One of the main conceptual weakness of the model discussed in Section 4 lies in its lack of an explicit, physically motivated prescription for star formation processes caused by the absence of a dedicated treatment of the ISM. Star formation is instead fully described by equation (B3), which simply states that the material that does not feed the BH gets partitioned into stars and recycled gas. In other words, the BH is the preferential target for gas accretion, and only the cold gas spared by BH feeding – if AGN feedback permits – participates in star formation processes. While this prescription simplifies significantly the treatment of star formation in our model, it does not capture the commonly accepted idea that gas cooling from the circumgalactic medium is firstly deposited on to the ISM by different mechanisms (e.g. Marasco, Fraternali & Binney 2012; Fraternali 2017), and only later can participate to star formation and BH feeding processes depending on the complex physics of this medium. Also, since in our model we do not follow gas dynamics explicitly, we cannot address the question on how gas is transported from the scales of the circumgalactic medium (tens or hundreds of kpc) down to the scales of BH accretion discs ( $\sim 10^{-2}$  pc). Dedicated analytical and numerical models are required explore the physical processes responsible for gas transport to different scales (e.g. Hopkins & Quataert 2011).

The adopted prescription also does not allow us to follow the physics of star formation quenching, which is instead implemented ‘ad-hoc’ in the model: the time when the BH enters the self-regulated phase marks the end of the stellar mass built-up, as any subsequent inflow of gas will target the BH alone. This has a number of side effects. First, it produces a net segregation between star-forming and quenched systems (Fig. 7), leaving no space for a transitory, ‘green-valley’-like regime. Secondly, as the BH population keeps growing in mass while star formation is stopped, the  $M_{\text{BH-to-}M_*}$  ratio increases with time in most massive systems (panel d in Fig. 8), which is in tension with high- $z$  observations (e.g. Merloni et al. 2010). Thirdly, it leads to a SHMR that is slightly too steep in the high-mass end. This is only marginally visible from Fig. 6 but becomes much more evident when an isothermal equation of state ( $\gamma = 1$  in equation (B6)) is used, as discussed in Section 4.2. A model in which gas accretion gets partitioned *a priori* between star formation and BH feeding, in the delicate phase where  $E_{\text{BH}} \simeq E_{\text{cool}}$ , may help to alleviate these issues and would likely provide a more realistic picture of stellar and BH mass assembly in high-mass galaxies.

Our model assumes a continuous and smooth mass assembly, which begs the question if mergers play any role in it. The smooth accretion of dark matter and gas that we adopt (equation B1) can also be interpreted as a continuous ‘rain’ of gas-rich minor mergers, but we stress that in our framework the bulk of stellar and BH mass is built ‘*in situ*’. While cosmological hydrodynamical simulations suggest that most of the stellar mass in haloes with  $M_h > 10^{13} M_\odot$  is built *ex situ* (Pillepich et al. 2018b), which may also explain why  $M_{\text{bulge}}$  correlates with  $M_{\text{BH}}$  better than  $M_{\text{disc}}$ , a scenario where the BH scaling

relations are preferentially produced by mergers does not seem to be favoured by the data (King & Nealon 2021). However, major mergers may be relevant to set galaxy morphology, as discussed in Section 5.2.

Finally, we notice that the BH feedback efficiency adopted in our fiducial model,  $\epsilon_f = 1.0 \times 10^{-2}$ , is 5–10 times smaller than the typical values used in semi-analytical models (e.g. Croton et al. 2006, 2016) and cosmological hydrodynamical simulations (e.g. Di Matteo, Springel & Hernquist 2005; Schaye et al. 2015; Pillepich et al. 2018a) to reproduce galaxy scaling relations. It is not trivial to compare our feedback prescription with those adopted in these more complex models, which often employ different feedback ‘modes’ (e.g. ‘quasar’-mode and ‘radio’-mode) depending on the BH accretion rate. Also,  $\epsilon_f$  varies significantly from one model to another: for instance, in their hydrodynamical simulations, Valentini et al. (2020) implemented the coupling between the AGN energy and a realistic multiphase ISM, finding that  $\epsilon_f \sim 10^{-2}$  adequately regulates the BH growth in Milky Way-like galaxies. A simplification that we adopted here is the absence of an AGN duty cycle: our model assumes a continuous feeding of the BH, corresponding to a continuous energy output distributed over the entire galaxy lifespan, whereas the observed AGN activity is intermittent. We plan to take this effect into account in future developments of our model.

## 6 CONCLUSIONS

Galaxy formation is regulated by the competition between processes that favour the growth of stars and supermassive BHs, such as the cooling and gravitational collapse of gas accreted from the intergalactic medium, and those that quench them, namely negative feedback resulting from star formation and BH accretion. The stellar, halo, and BH masses of present-day galaxies are precious remnants of these evolutionary processes and of the key parameters that describe them. For these reasons, the characterization of the relations between  $M_{\text{BH}}$ ,  $M_h$ , and  $M_*$  (or equivalently, as in this study,  $f_*$ ) at any redshift is a subject of great interest for both the observational and the theoretical astrophysical communities.

In this work, we have focused on the relations between  $M_{\text{BH}}$ ,  $M_h$ , and  $f_*$  at  $z \sim 0$  using a sample of 55 galaxies with dynamical estimates of their BH and halo masses, all having  $M_{\text{BH}} > 10^6 M_\odot$  and  $M_h > 5 \times 10^{11} M_\odot$ . Unlike previous studies, where the line-widths of the integrated velocity profiles from H I, CO or H $\alpha$  data were used as proxies for  $M_h$  (e.g. Sabra et al. 2015; Davis et al. 2019b; Smith et al. 2021), our sample is almost entirely made of galaxies for which either spatially resolved rotation curves or globular cluster kinematics were previously analysed in the literature, providing a more refined estimate of their  $M_h$ . Our main results, valid in the mass range considered, can be summarized as follows:

- (i)  $M_h$  and  $M_{\text{BH}}$  strongly correlate with each other and anticorrelate with  $f_*$  (Fig. 1). In general, galaxies tend to follow a 1D sequence in the  $M_h - M_{\text{BH}} - f_*$  space, rather than distributing across a 2D plane (Fig. 3).
- (ii) In our sample, the strength and tightness of the correlation between  $M_{\text{BH}}$  and  $M_h$  is comparable to the one between  $M_{\text{BH}}$  and  $\sigma_e$ , the mean stellar velocity dispersion within the effective radius (Fig. 4).
- (iii) Bulge masses correlates with  $M_{\text{BH}}$  significantly better than disc masses, but not statistically better than the total  $M_*$  of the host galaxy. The limitations of our sample prevent us from assessing whether this property is also applicable to a complete, volume-limited sample.

(iv) The slopes of the  $M_{\text{BH}}-M_{\text{h}}$  and the  $f_{\star}-M_{\text{BH}}$  relations show a break at  $M_{\text{h}} \sim 10^{12} M_{\odot}$  or  $M_{\text{BH}} \sim 10^7-10^8 M_{\odot}$  (Fig. 1).

(v) At a fixed  $M_{\text{BH}}, f_{\star}$  correlates negatively with  $M_{\text{h}}$  and positively with the Hubble morphological T-type. That is, at a given BH mass, galaxies with a higher global star formation efficiency tend to have later morphological types and to occupy less massive haloes (Figs 6 and 2). There is no significant trend instead between  $M_{\text{BH}}$  and  $f_{\star}$  at fixed  $M_{\text{h}}$ .

In Section 5, we developed an equilibrium model in the  $\Lambda$ CDM framework to explain the observed trends and provide insights into their physical origin. Our model, largely inspired by that developed by B17, assumes that galaxies evolve by smoothly accreting dark and baryonic matter at a cosmological rate, while the competition between the cooling of the available gas reservoir and negative feedback from star formation and AGN regulates the growth rates of stars and BHs. The model is based on five free parameters regulating the stellar and AGN feedback, which we manually tuned to match the data. In spite of its simplicity, the model reproduces the observed relations remarkably well, including the break at  $M_{\text{BH}} \sim 10^7-10^8 M_{\odot}$  and the trends found at fixed  $M_{\text{BH}}$  and  $M_{\text{h}}$  (Figs 6 and 11). In the model, the break originates as the BH population transits from a rapidly accreting phase, in which stellar feedback is inefficient and the BH feedback energy  $E_{\text{BH}}$  is still small compared to the gravitational binding energy of the cooling gas  $E_{\text{cool}}$ , to a more gradual and self-regulated growth, driven by the continuous balance between the  $E_{\text{BH}}$  and  $E_{\text{cool}}$ . This balance produces a slope in the  $M_{\text{BH}}-M_{\text{h}}$  relation in excellent agreement with the data at  $M_{\text{h}} > 10^{12} M_{\odot}$ . The correlations at fixed  $M_{\text{BH}}$  are instead produced by scatter in the BH feedback efficiency: higher efficiencies lead to less massive BHs at a given halo mass but do not alter the SHMR; hence, at fixed  $M_{\text{BH}}$ , galaxies with a higher  $f_{\text{star}}$  will be those occupying less massive haloes.

As our model lacks a dedicated treatment of mass accretion provided by mergers, it does not allow us to follow separately the formation of spheroids and discs, which in turns prevents us from drawing conclusions on the physics that regulate the co-evolution between spheroids and BHs. More advanced models are required to tackle this topic, which we plan to implement in a follow-up study.

## ACKNOWLEDGEMENTS

The authors thank Alister Graham for providing constructive comments to the manuscript. AM and GC acknowledge the support by INAF/Frontiera through the ‘Progetti Premiali’ funding scheme of the Italian Ministry of Education, University, and Research. LP acknowledges support from the Centre National d’Études Spatiales (CNES) and from the European Research Council (ERC) under the European Unions Horizon 2020 research and innovation program (grant agreement no. 834148).

## DATA AVAILABILITY

The data underlying this article are available in the article and in its online supplementary material.

## REFERENCES

Bacchini C., Fraternali F., Iorio G., Pezzulli G., Marasco A., Nipoti C., 2020, *A&A*, 641, A70  
 Bajaja E., van der Burg G., Faber S. M., Gallagher J. S., Knapp G. R., Shane W. W., 1984, *A&A*, 141, 309

Baldry I. K., Glazebrook K., Brinkmann J., Ivezić Ž., Lupton R. H., Nichol R. C., Szalay A. S., 2004, *ApJ*, 600, 681  
 Bandara K., Crampton D., Simard L., 2009, *ApJ*, 704, 1135  
 Behroozi P. S., Conroy C., Wechsler R. H., 2010, *ApJ*, 717, 379  
 Behroozi P. S., Wechsler R. H., Conroy C., 2013, *ApJ*, 770, 57  
 Behroozi P., Wechsler R. H., Hearin A. P., Conroy C., 2019, *MNRAS*, 488, 3143  
 Berrier J. C. et al., 2013, *ApJ*, 769, 132  
 Binney J., Nipoti C., Fraternali F., 2009, *MNRAS*, 397, 1804  
 Boardman N. F. et al., 2016, *MNRAS*, 460, 3029  
 Bondi H., 1952, *MNRAS*, 112, 195  
 Booth C. M., Schaye J., 2010, *MNRAS*, 405, L1  
 Bouché N. et al., 2010, *ApJ*, 718, 1001  
 Bower R. G., Schaye J., Frenk C. S., Theuns T., Schaller M., Crain R. A., McAlpine S., 2017, *MNRAS*, 465, 32 (B17)  
 Braun R., Walterbos R. A. M., Kennicutt R. C. J., Tacconi L. J., 1994, *ApJ*, 420, 558  
 Brodie J. P. et al., 2014, *ApJ*, 796, 52  
 Brook C. B., Santos-Santos I., Stinson G., 2016, *MNRAS*, 459, 638  
 Bruzual G., Charlot S., 2003, *MNRAS*, 344, 1000  
 Bundy K. et al., 2008, *ApJ*, 681, 931  
 Cappellari M. et al., 2013, *MNRAS*, 432, 1709  
 Chemin L., Cayatte V., Balkowski C., Marcelin M., Amram P., van Driel W., Flores H., 2003, *A&A*, 405, 89  
 Chen Z. et al., 2020, *ApJ*, 897, 102  
 Corbelli E., Lorenzoni S., Walterbos R., Braun R., Thilker D., 2010, *A&A*, 511, A89  
 Correa C. A., Wyithe J. S. B., Schaye J., Duffy A. R., 2015, *MNRAS*, 450, 1521  
 Côté P., McLaughlin D. E., Cohen J. G., Blakeslee J. P., 2003, *ApJ*, 591, 850  
 Cowie L. L., Songaila A., Hu E. M., Cohen J. G., 1996, *AJ*, 112, 839  
 Croton D. J. et al., 2006, *MNRAS*, 365, 11  
 Croton D. J. et al., 2016, *ApJS*, 222, 22  
 Davis B. L., Graham A. W., Seigar M. S., 2017, *MNRAS*, 471, 2187  
 Davis B. L., Graham A. W., Cameron E., 2018, *ApJ*, 869, 113  
 Davis B. L., Graham A. W., Cameron E., 2019a, *ApJ*, 873, 85  
 Davis B. L., Graham A. W., Combes F., 2019b, *ApJ*, 877, 64  
 Davis S. W., Laor A., 2011, *ApJ*, 728, 98  
 Dayal P., Rossi E. M., Shiralilou B., Piana O., Choudhury T. R., Volonteri M., 2019, *MNRAS*, 486, 2336  
 de Blok W. J. G., Walter F., Brinks E., Trachternach C., Oh S. H., Kennicutt R. C. J., 2008, *AJ*, 136, 2648  
 de Nicola S., Marconi A., Longo G., 2019, *MNRAS*, 490, 600  
 Dekel A., Birnboim Y., 2006, *MNRAS*, 368, 2  
 Dekel A., Silk J., 1986, *ApJ*, 303, 39  
 Di Matteo T., Springel V., Hernquist L., 2005, *Nature*, 433, 604  
 Dubois Y., Gavazzi R., Peirani S., Silk J., 2013, *MNRAS*, 433, 3297  
 Dutton A. A., Conroy C., van den Bosch F. C., Prada F., More S., 2010, *MNRAS*, 407, 2  
 Dutton A. A., Macciò A. V., 2014, *MNRAS*, 441, 3359  
 Emsellem E., Fathi K., Wozniak H., Ferruit P., Mundell C. G., Schinnerer E., 2006, *MNRAS*, 365, 367  
 Erroz-Ferrer S. et al., 2015, *MNRAS*, 451, 1004  
 Erwin P., Thomas J., Saglia R. P., Fabricius M., Rusli S. P., Seitz S., Bender R., 2018, *MNRAS*, 473, 2251  
 Eyles L. P., Bunker A. J., Stanway E. R., Lacy M., Ellis R. S., Doherty M., 2005, *MNRAS*, 364, 443  
 Faber S. M., Jackson R. E., 1976, *ApJ*, 204, 668  
 Fall S. M., Efstathiou G., 1980, *MNRAS*, 193, 189  
 Fall S. M., Romanowsky A. J., 2018, *ApJ*, 868, 133  
 Ferrarese L., 2002, *ApJ*, 578, 90  
 Fisher D., 1997, *AJ*, 113, 950  
 Fontanot F., De Lucia G., Monaco P., Somerville R. S., Santini P., 2009, *MNRAS*, 397, 1776  
 Forbes D. A. et al., 2017, *AJ*, 153, 114  
 Fraternali F., 2017, Gas Accretion via Condensation and Fountains. p. 323  
 Fraternali F., Tomassetti M., 2012, *MNRAS*, 426, 2166

- García-Barreto J. A., Combes F., Koribalski B., Franco J., 1999, *A&A*, 348, 685
- Geha M., Blanton M. R., Yan R., Tinker J. L., 2012, *ApJ*, 757, 85
- Graham A. W., 2016, in Laurikainen E., Peletier R., Gadotti D., eds, *Galaxy Bulges*. Springer Int. Publ., Cham, p. 263
- Graham A. W., Scott N., 2013, *ApJ*, 764, 151
- Gültekin K., Gebhardt K., Kormendy J., Lauer T. R., Bender R., Tremaine S., Richstone D. O., 2014, *ApJ*, 781, 112
- Guo Q., White S., Angulo R. E., Henriques B., Lemson G., Boylan-Kolchin M., Thomas P., Short C., 2013, *MNRAS*, 428, 1351
- Haehnelt M. G., Natarajan P., Rees M. J., 1998, *MNRAS*, 300, 817
- Harrison C. M., 2017, *Nat. Astron.*, 1, 0165
- Henriques B. M. B., White S. D. M., Thomas P. A., Angulo R., Guo Q., Lemson G., Springel V., Overzier R., 2015, *MNRAS*, 451, 2663
- Hopkins P. F., Hernquist L., Cox T. J., Di Matteo T., Robertson B., Springel V., 2006, *ApJS*, 163, 1
- Hopkins P. F. et al., 2010, *ApJ*, 715, 202
- Hopkins P. F., Quataert E., 2011, *MNRAS*, 415, 1027
- Hopkins P. F., Wellons S., Angles-Alcazar D., Faucher-Giguere C.-A., Grudic M. Y., 2021, preprint ([arXiv:2103.10444](https://arxiv.org/abs/2103.10444))
- Huchra J. P. et al., 2012, *ApJS*, 199, 26
- Jahnke K., Macciò A. V., 2011, *ApJ*, 734, 92
- Jones K. L., Koribalski B. S., Elmouttie M., Haynes R. F., 1999, *MNRAS*, 302, 649
- Katz H., Desmond H., McGaugh S., Lelli F., 2019, *MNRAS*, 483, L98
- Kelvin L. S. et al., 2014, *MNRAS*, 444, 1647
- Kereš D., Katz N., Weinberg D. H., Davé R., 2005, *MNRAS*, 363, 2
- Kim D. W., Guhathakurta P., van Gorkom J. H., Jura M., Knapp G. R., 1988, *ApJ*, 330, 684
- King A., 2003, *ApJ*, 596, L27
- King A., Nealon R., 2021, *MNRAS*, 502, L1
- King A., Pounds K., 2015, *ARA&A*, 53, 115
- Kormendy J., Bender R., 2011, *Nature*, 469, 377
- Kormendy J., Gebhardt K., 2001, in Wheeler J. C., Martel H., eds, *AIP Conf. Ser. Vol. 586, 20th Texas Symposium on relativistic astrophysics*. Am. Inst. Phys., New York, p. 363
- Kormendy J., Ho L. C., 2013, *ARA&A*, 51, 511
- Krajinović D. et al., 2018, *MNRAS*, 477, 3030
- Kravtsov A. V., Vikhlinin A. A., Meshcheryakov A. V., 2018, *Astron. Lett.*, 44, 8
- Kroupa P., Subr L., Jerabkova T., Wang L., 2020, *MNRAS*, 498, 5652
- Krumpe M., Miyaji T., Husemann B., Fanidakis N., Coil A. L., Aceves H., 2015, *ApJ*, 815, 21
- Lamastra A., Menci N., Maiolino R., Fiore F., Merloni A., 2010, *MNRAS*, 405, 29
- Larson R. B., 1974, *MNRAS*, 169, 229
- Läsker R., Ferrarese L., van de Ven G., Shankar F., 2014, *ApJ*, 780, 70
- Lauer T. R., Tremaine S., Richstone D., Faber S. M., 2007, *ApJ*, 670, 249
- Leauthaud A. et al., 2012, *ApJ*, 744, 159
- Lelli F., McGaugh S. S., Schombert J. M., 2016, *AJ*, 152, 157
- Lilly S. J., Carollo C. M., Pipino A., Renzini A., Peng Y., 2013, *ApJ*, 772, 119
- Lindblad P. A. B., Kristen H., Joersaeter S., Hoegbom J., 1997, *A&A*, 317, 36
- Loeb A., Rasio F. A., 1994, *ApJ*, 432, 52
- Magorrian J. et al., 1998, *AJ*, 115, 2285
- Mandelbaum R., Seljak U., Kauffmann G., Hirata C. M., Brinkmann J., 2006, *MNRAS*, 368, 715
- Marasco A., Debattista V. P., Fraternali F., van der Hulst T., Wadsley J., Quinn T., Roškar R., 2015, *MNRAS*, 451, 4223
- Marasco A., Fraternali F., Binney J. J., 2012, *MNRAS*, 419, 1107
- Marconi A., Hunt L. K., 2003, *ApJ*, 589, L21
- Marconi A., Risaliti G., Gilli R., Hunt L. K., Maiolino R., Salvati M., 2004, *MNRAS*, 351, 169
- Martin G., Kaviraj S., Devriendt J. E. G., Dubois Y., Pichon C., 2018, *MNRAS*, 480, 2266
- McConnell N. J., Ma C.-P., 2013, *ApJ*, 764, 184
- McGaugh S. S., Schombert J. M., 2014, *AJ*, 148, 77
- Memola E., Salucci P., Babić A., 2011, *A&A*, 534, A50
- Merloni A. et al., 2010, *ApJ*, 708, 137
- Mo H. J., Mao S., White S. D. M., 1998, *MNRAS*, 295, 319
- Moore E. M., Gottesman S. T., 1995, *ApJ*, 447, 159
- More S., van den Bosch F. C., Cacciato M., Skibba R., Mo H. J., Yang X., 2011, *MNRAS*, 410, 210
- Moster B. P., Naab T., White S. D. M., 2013, *MNRAS*, 428, 3121
- Mundell C. G., Pedlar A., Axon D. J., Meaburn J., Unger S. W., 1995, *MNRAS*, 277, 641
- Mundell C. G., Pedlar A., Shone D. L., Robinson A., 1999, *MNRAS*, 304, 481
- Mutlu-Pakdil B., Seigar M. S., Hewitt I. B., Treuhardt P., Berrier J. C., Koval L. E., 2018, *MNRAS*, 474, 2594
- Muzzin A. et al., 2013, *ApJ*, 777, 18
- Navarro J. F., Frenk C. S., White S. D. M., 1996, *ApJ*, 462, 563
- Nehlig F., Vollmer B., Braine J., 2016, *A&A*, 587, A108
- Noeske K. G. et al., 2007, *ApJ*, 660, L43
- Noordermeer E., van der Hulst J. M., Sancisi R., Swaters R. S., van Albada T. S., 2007, *MNRAS*, 376, 1513
- Norris M. A. et al., 2012, *MNRAS*, 421, 1485
- Ondrechen M. P., van der Hulst J. M., Hummel E., 1989, *ApJ*, 342, 39
- Peng C. Y., 2007, *ApJ*, 671, 1098
- Peng C. Y., Ho L. C., Impey C. D., Rix H.-W., 2002, *AJ*, 124, 266
- Peng C. Y., Ho L. C., Impey C. D., Rix H.-W., 2010a, *AJ*, 139, 2097
- Peng Y.-j. et al., 2010b, *ApJ*, 721, 193
- Pillepich A. et al., 2018a, *MNRAS*, 473, 4077
- Pillepich A. et al., 2018b, *MNRAS*, 475, 648
- Pizzella A., Corsini E. M., Dalla Bontà E., Sarzi M., Coccatto L., Bertola F., 2005, *ApJ*, 631, 785
- Planck Collaboration XVI, 2014, *A&A*, 571, A16
- Ponomareva A. A., Verheijen M. A. W., Bosma A., 2016, *MNRAS*, 463, 4052
- Ponomareva A. A., Verheijen M. A. W., Peletier R. F., Bosma A., 2017, *MNRAS*, 469, 2387
- Popesso P. et al., 2019, *MNRAS*, 483, 3213
- Posti L., Fall S. M., 2021, *A&A*, 649, A119 (PF21)
- Posti L., Helmi A., 2019, *A&A*, 621, A56
- Posti L., Fraternali F., Marasco A., 2019a, *A&A*, 626, A56
- Posti L., Marasco A., Fraternali F., Famaey B., 2019b, *A&A*, 629, A59
- Power C., Zubovas K., Nayakshin S., King A. R., 2011, *MNRAS*, 413, L110
- Pu S. B., Saglia R. P., Fabricius M. H., Thomas J., Bender R., Han Z., 2010, *A&A*, 516, A4
- Read J. I., Iorio G., Agertz O., Fraternali F., 2017, *MNRAS*, 467, 2019
- Renzini A., Peng Y.-j., 2015, *ApJ*, 801, L29
- Roberts M. S., Haynes M. P., 1994, *ARA&A*, 32, 115
- Robinson J. H. et al., 2021, *ApJ*, 912, 160
- Romeo A. B., Agertz O., Renaud F., 2020, *MNRAS*, 499, 5656
- Sabra B. M., Saliba C., Abi Akl M., Chahine G., 2015, *ApJ*, 803, 5
- Saglia R. P. et al., 2016, *ApJ*, 818, 47
- Sahu N., Graham A. W., Davis B. L., 2019a, *ApJ*, 876, 155
- Sahu N., Graham A. W., Davis B. L., 2019b, *ApJ*, 887, 10
- Savorgnan G. A. D., Graham A. W., Marconi A., Sani E., 2016, *ApJ*, 817, 21
- Schaye J. et al., 2015, *MNRAS*, 446, 521
- Schuberth Y., Richtler T., Hilker M., Dirsch B., Bassino L. P., Romanowsky A. J., Infante L., 2010, *A&A*, 513, A52
- Scott N., Graham A. W., Schombert J., 2013, *ApJ*, 768, 76
- Seigar M. S., Kennefick D., Kennefick J., Lacy C. H. S., 2008, *ApJ*, 678, L93
- Sersic J. L., 1968, *Atlas de galaxias australes Observatorio Astronomico. Universidad Nacional de Cordoba, Cordoba*
- Sheth K. et al., 2010, *PASP*, 122, 1397
- Shostak G. S., 1987, *A&A*, 175, 4
- Silk J., Rees M. J., 1998, *A&A*, 331, L1
- Smith M. D. et al., 2021, *MNRAS*, 500, 1933
- Sofue Y., Tutui Y., Honma M., Tomita A., Takamiya T., Koda J., Takeda Y., 1999, *ApJ*, 523, 136
- Soltan A., 1982, *MNRAS*, 200, 115
- Somerville R. S., Davé R., 2015, *ARA&A*, 53, 51

- Somerville R. S., Hopkins P. F., Cox T. J., Robertson B. E., Hernquist L., 2008, *MNRAS*, 391, 481
- Speights J. C., Godwin C., Reimer R., Benton A., Lemaire R., 2019, *ApJ*, 883, 77
- Sun A.-L., Greene J. E., Impellizzeri C. M. V., Kuo C.-Y., Braatz J. A., Tuttle S., 2013, *ApJ*, 778, 47
- Sutherland R. S., Dopita M. A., 1993, *ApJS*, 88, 253
- Terrazas B. A., Bell E. F., Woo J., Henriques B. M. B., 2017, *ApJ*, 844, 170
- Trinchieri G., Marino A., Mazzei P., Rampazzo R., Wolter A., 2012, *A&A*, 545, A140
- Tully R. B., Fisher J. R., 1977, *A&A*, 500, 105
- Vale A., Ostriker J. P., 2004, *MNRAS*, 353, 189
- Valentini M. et al., 2020, *MNRAS*, 491, 2779
- van Albada T. S., Sancisi R., 1986, *Phil. Trans. R. Soc.*, 320, 447
- van den Bosch F. C., Lange J. U., Zentner A. R., 2019, *MNRAS*, 488, 4984
- van den Bosch R. C. E., 2016, *ApJ*, 831, 134
- vanGorkom J. H., van der Hulst J. M., Haschick A. D., Tubbs A. D., 1990, *AJ*, 99, 1781
- Veilleux S., Bland-Hawthorn J., Cecil G., 1999, *AJ*, 118, 2108
- Vogelsberger M. et al., 2014, *MNRAS*, 444, 1518
- Volonteri M., Natarajan P., Gültekin K., 2011, *ApJ*, 737, 50
- Wechsler R. H., Tinker J. L., 2018, *ARA&A*, 56, 435
- White S. D. M., Frenk C. S., 1991, *ApJ*, 379, 52
- White S. D. M., Rees M. J., 1978, *MNRAS*, 183, 341
- Whitmore B. C., Kirshner R. P., 1981, *ApJ*, 250, 43
- Whitmore B. C., Kirshner R. P., Schechter P. L., 1979, *ApJ*, 234, 68
- Wolfire M. G., McKee C. F., Hollenbach D., Tielens A. G. G. M., 2003, *ApJ*, 587, 278
- Woods D., Madore B. F., Fahlman G. G., 1990, *ApJ*, 353, 90
- Zasov A. V., Khoperskov A. V., Katkov I. Y., Afanasiev V. L., Kaisin S. S., 2012, *Astrophys. Bull.*, 67, 362
- Zinger E. et al., 2020, *MNRAS*, 499, 768

## APPENDIX A: THE CONVERSION FROM $v_{\text{FLAT}}$ TO $M_{\text{H}}$

In Section 2, we make use of rotation curve measurements to estimate  $M_{\text{h}}$  in our systems. Rather than resorting to theoretical models, we prefer to calibrate the  $M_{\text{h}}-v_{\text{flat}}$  relation empirically using the results of Posti et al. (2019a), which are based on mass decomposition

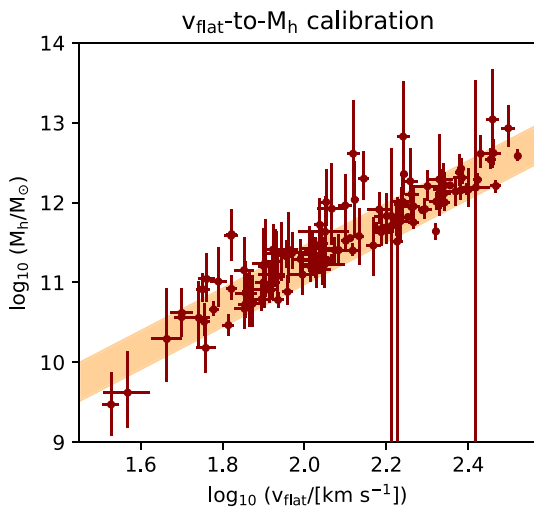


**Figure A1.** Relation between  $M_{\text{h}}$  and  $v_{\text{flat}}$  for a sample of 125 disc galaxies from the SPARC sample (Lelli et al. 2016), as derived from the mass modeling of their rotation curves from Posti et al. (2019a). The shaded region shows a linear fit to the data and its rms scatter around it, and is used as a calibrator for the  $v_{\text{flat}}-M_{\text{h}}$  conversion in our sample.

of rotation curves from the SPARC galaxy sample (Lelli et al. 2016).

In Fig. A1, we show that this relation holds over a large dynamical range, and is given by

$$\log_{10} \left( \frac{M_{\text{h}}}{M_{\odot}} \right) = (5.93 \pm 0.02) + (2.65 \pm 0.07) \log_{10} \left( \frac{v_{\text{flat}}}{\text{km s}^{-1}} \right), \quad (\text{A1})$$

with an rms scatter of 0.24 dex, which we adopt as the uncertainty associated to our  $M_{\text{h}}$  estimates via equation (A1). The final uncertainty also incorporates measurement errors in  $v_{\text{flat}}$ . These, however, are often very small or not quoted at all in the literature.

We note that similar relations for the SPARC sample were recently derived by Katz et al. (2019) using a variety of different assumptions in the rotation curve decomposition procedures. In Katz et al. (2019), the values for the slope (intercept) of equation (A1) vary in the range 2.2–2.9 (5.3–6.9), depending on the halo profile adopted and on the priors used in the modeling. Our estimates in equation (A1) are well within these ranges.

## APPENDIX B: DETAILED MODEL DESCRIPTION

In this appendix, we describe in detail our theoretical model of galaxy evolution used in Section 4. For consistency with the observed data set, we assume that all halo ‘virial’ quantities (such as mass, radius, and velocity) are defined at (or within)  $r_{200}^{\text{crit}}$ , the radius where the mean halo density becomes equal to 200 times the (redshift-dependant) critical density of the Universe, and simply use the suffix ‘h’ to refer to halo properties.

### Halo growth

We start by assuming a cosmological growth for dark matter haloes as parametrized by Correa et al. (2015)<sup>4</sup>:

$$\frac{\dot{M}_{\text{h}}}{M_{\odot} \text{ Gyr}^{-1}} = 7.16 \times 10^{10} h_{07} \left( \frac{M_{\text{h}}}{10^{12} M_{\odot}} \right) \times [-0.24 + 0.75(1+z)] \Delta_z^{3/2}, \quad (\text{B1})$$

where  $h_{07} \equiv H_0/(70 \text{ km s}^{-1} \text{ Mpc}^{-1})$ ,  $H_0$  is the Hubble constant, and  $\Delta_z \equiv (\Omega_{\text{m}}(1+z)^3 + \Omega_{\Lambda})^{1/3}$  (so that the Hubble parameter  $H(z)$  is given by  $H_0 \Delta_z^{3/2}$ ).

Equation (B1), like the other equations in this appendix, is solved numerically from  $t = t_{\text{seed}}$  to  $t = 13.8 \text{ Gyr}$ , corresponding to the current age of the Universe, using a constant time-step  $\delta t$  of 10 Myr and assuming  $M_{\text{h}}(t = t_{\text{seed}}) = 10^{10} M_{\odot}$ . By varying  $t_{\text{seed}}$  from 0.3 Gyr to 4 Gyr, we can sample halo masses at the present epoch from  $10^{10.5} M_{\odot}$  (for younger seeds) to  $10^{14} M_{\odot}$  (for older seeds). We note that varying the seed halo mass is equivalent of varying the seed time, and simply allows us to modify the range of  $M_{\text{h}}$  sampled at  $z = 0$  with no consequences on our results.

Halos accrete baryons as well as dark matter. At any given time  $t$ , the total baryonic content of our system is always  $f_{\text{b}} M_{\text{h}}(t)$ ,  $f_{\text{b}}$  being the universal baryonic fraction. This material is divided into gas, stars, and BH as described below.

<sup>4</sup>Note that this parametrization is valid for  $M_{\text{h}} \equiv M_{200}^{\text{crit}}$ , as we assume here.

### Gas cooling

We assume that, at any given time  $t$ , the total gas reservoir of our model galaxy is given by  $M_{\text{gas}}(t) = f_b M_h(t) - M_*(t) - M_{\text{BH}}(t)$ ,  $M_*(t)$  and  $M_{\text{BH}}(t)$  being the stellar and BH mass of the galaxy. In reality, this gaseous reservoir is a complex, multiphase structure build by a mixture of heterogeneous processes, including cosmological accretion of pristine gas, outflows produced by stellar and BH feedback. Our model does not aim to capture the complex physics of this medium. We make instead the simplifying assumption that the entire reservoir is in a single phase defined by the virial temperature  $T_h$  of the dark matter halo. Therefore, in what follows, we make no distinction between ISM and CGM, and simply refer to the whole gas reservoir as the ‘gas’ component of the model.

Clearly, only a small fraction of  $M_{\text{gas}}$  can be used to form stars and to feed the BH, and we assume that this fraction is determined by the cooling rate of the gas reservoir. Specifically, following White & Frenk (1991), at any time  $t$ , we define the halo cooling radius  $r_{\text{cool}}$  as the radius within a halo where the cooling time is equal to  $t$ . Using the formulation from Chen et al. (2020), we have

$$r_{\text{cool}} = \min \left\{ r_h, \left( \frac{M_{\text{gas}} \Lambda(T_h, Z)}{4\pi \mu m_p (\frac{3}{2} k_B T_h v_h)} \right)^{1/2} \right\} \quad (\text{B2})$$

where  $r_h$ ,  $T_h$ , and  $v_h$  are the halo virial radius, temperature, and circular velocity measured at  $r_h$ , respectively,  $\Lambda(T_h, Z_{\text{gas}})$  is the cooling function ( $Z_{\text{gas}}$  being the gas metallicity),  $k_B$  is the Boltzmann constant, and  $m_p$  is the proton mass. In this work, we use the collisional ionization equilibrium cooling functions of Sutherland & Dopita (1993) at metallicity  $Z_{\text{gas}} = 0$ , representative for a pristine gas. In Section 4.2, we explore the effect of using a higher metallicity.

The ratio  $r_{\text{cool}}/r_h$  is a decreasing function of both cosmic time and  $M_h$ . At high  $z$ , where halo masses are small, densities are high, and gas can efficiently cool,  $r_{\text{cool}}/r_h = 1$  in all systems. As time progresses, haloes grow and cooling remains efficient only within a fraction of the virial radius, but in the lowest mass regime ( $M_h(z=0) \lesssim 2 \times 10^{11} M_\odot$ ), the ratio remains 1 even at  $z=0$ . This is related to the dichotomy between the so-called ‘cold’ and ‘hot’ mode gas accretion (e.g. Kereš et al. 2005; Dekel & Birnboim 2006), with the former (latter) working preferentially at high (low)  $z$  and in low-mass (high-mass) systems. In present-day Milky-Way-like galaxies,  $r_{\text{cool}}/r_h$  decreases below 1 at  $z \sim 4$ .

Assuming NFW profiles and the time-dependent  $M_h$ –concentration relation from Dutton & Macciò (2014), we can compute  $f_{\text{cool}}$ , the mass fraction enclosed within  $r_{\text{cool}}$ , and the total mass of the cooling gas  $M_{\text{cool}}$  as  $f_{\text{cool}} M_{\text{gas}}$ . The time-derivative of this quantity,  $\dot{M}_{\text{cool}}$ , gives the rate that becomes gas eligible for star formation and BH feeding at any given time.

We implicitly assume that the dominant time-scale of the gas accretion process is the gas cooling time (e.g. Binney, Nipoti & Fraternali 2009), and that the newly cooled material can be used immediately by the galaxy with no delay time, that is  $t_{\text{dyn}} \ll t_{\text{cool}}$ .

### Stellar growth and feedback

We assume a simple equilibrium model where the rate at which the gas cools is balanced by the rates at which stars form, the BH grows and gas is returned to the initial reservoir because of stellar mass losses and feedback. Such a model can be described by

$$\dot{M}_{\text{cool}} = \dot{M}_{\text{BH}} + (1 - \mathcal{R} + \beta) \dot{M}_* \quad (\text{B3})$$

where  $\mathcal{R}$  is the recycled gas fraction due to stellar mass losses and  $\beta$  is the mass-loading factor of the outflows driven by stellar feedback. Here, we set  $\mathcal{R} = 0.3$  (e.g. Fraternali & Tomassetti 2012), but similar results can be obtained using  $\mathcal{R} = 0.5$  (Bruzual & Charlot 2003) by slightly adjusting the model parameters. The parameter  $\beta$ , instead, requires a more in-depth discussion.

Following an approach that is very popular in semi-analytical models, and is supported by arguments based on energy- and momentum-driven winds, we assume that  $\beta$  is a decreasing function of  $M_h$  (e.g. Somerville & Davé 2015, and references therein). This choice leads to a scenario where stellar feedback is very efficient in the low-mass regime, leading to low star formation efficiencies, but becomes less effective at larger masses. We parametrize the mass-loading factor as

$$\beta = \left( \frac{M_h}{M_{\text{crit}}} \right)^{-\alpha} \quad (\text{B4})$$

with  $\alpha > 0$ . In equation (B4),  $M_{\text{crit}}$  is a time-dependent critical mass below which stellar feedback is more effective. As in B17 and Dayal et al. (2019), we assume that  $M_{\text{crit}}$  scales with redshift as

$$M_{\text{crit}} = M_{\text{crit},0} \Delta_z^{-3/8} \quad (\text{B5})$$

where  $M_{\text{crit},0}$  sets the critical mass at  $z=0$ . We notice that the redshift dependence in equation (B5) is very weak:  $\Delta_z^{-3/8} = 1$  at  $z=0$ ,  $\sim 0.76$  at  $z=2$  and  $\sim 0.59$  at  $z=5$ . In B17,  $\alpha$  is fixed to 8/9 and  $M_{\text{crit},0}$  to  $10^{12} M_\odot$ , while Dayal et al. (2019) adopt  $M_{\text{crit},0} = 10^{11.25} M_\odot$ . In this work, we prefer to treat both  $\alpha$  and  $M_{\text{crit},0}$  as free parameters.

Equation (B3) can be used to compute the stellar mass growth in the time interval  $[t, t + \delta t]$  if the BH mass growth is known. We describe how the latter is determined below. While a starting seed  $M_{*,\text{seed}} \equiv M_*(t = t_{\text{seed}})$  is required to integrate equation (B3), in practice we find that systems quickly lose memory of their initial seed and converge towards a stable solution for any reasonable choice of  $M_{*,\text{seed}}$ .  $M_{*,\text{seed}}$  has some impact on systems with present-day  $M_h < 10^{10.5} M_\odot$  but, in the range of masses studied here, can be considered only a technical necessity due to our implementation and has no particular physical meaning. For simplicity, we set  $M_{*,\text{seed}} = 10^3 \times M_{\text{BH},\text{seed}}$ .

In our model, feedback-driven outflows (via  $\beta$ ) and stellar mass losses (via  $\mathcal{R}$ ) immediately re-join the gas reservoir (so that the total baryonic mass within the virial radius remains  $f_b M_h$ ) and can participate in future stellar and BH growth.

### BH growth and feedback

We assume Bondi-like accretion (Bondi 1952), where the BH grows at a rate

$$\dot{M}_{\text{BH}} = 4\pi G^2 \frac{M_{\text{BH}}^2 \rho_{\text{BH}}}{c_s^3} \quad (\text{B6})$$

where  $G$  is the gravitational constant,  $\rho_{\text{BH}}$  is the density of the gas near the BH (ideally measured at the Bondi radius), and  $c_s$  is the gas effective sound speed. Equation (B6) represents a specific expression to parametrize the BH accretion as a function of BH mass and the thermo-dynamic properties of the gas, and has been largely adopted in the literature using different normalization factors (e.g. Di Matteo et al. 2005; Croton et al. 2006; Bower et al. 2017). We stress that different prescriptions are also possible (e.g. Hopkins & Quataert 2011), and that the mode by which BHs grow in the early Universe can be significantly different (e.g. Kroupa et al. 2020).

By adopting a polytropic equation of state  $P_{\text{BH}} \propto \rho_{\text{BH}}^\gamma$ ,  $P_{\text{BH}}$  being the gas pressure, equation (B6) can be written as

$$\dot{M}_{\text{BH}} = 4\pi G^2 \left( \frac{\mu m_p \rho_{\text{eos}}^{\gamma-1}}{\gamma k_B T_{\text{eos}}} \right)^{3/2} M_{\text{BH}}^2 \rho_{\text{BH}}^{(5-3\gamma)/2} \quad (\text{B7})$$

where  $\mu = 0.6$  is the gas mean atomic weight,  $m_p$  is the proton mass,  $k_B$  is the Boltzmann constant, and  $\rho_{\text{eos}}$  and  $T_{\text{eos}}$  define the normalization of the equation of state. Here, for simplicity, we adopt  $T_{\text{eos}} = 8000$  K and  $\rho_{\text{eos}}/\mu m_p = 0.375$  cm $^{-3}$ , meaning that, at the temperatures typical for the warm ISM, the pressure  $P_{\text{eos}}/k_B$  is 3000 K cm $^{-3}$ , similar to that determined for the Galactic ISM (Wolfire et al. 2003). However, we stress that any choice for  $T_{\text{eos}}$  or  $\rho_{\text{eos}}$  is degenerate with the normalization of  $\rho_{\text{BH}}$  defined below in equation (B8), thus the exact values of these quantities cannot be constrained by our analysis. For consistency with B17, we adopt  $\gamma = 4/3$ , so that  $\dot{M}_{\text{BH}} \propto M_{\text{BH}}^2 \rho_{\text{BH}}^{1/2}$ . Thus the BH growth will strongly depend on the BH seed mass, which is another free parameter of our model, and weakly on the gas density, which we model as described below. The isothermal case ( $\gamma = 1$ ) is briefly discussed in Section 4.2.

As in B17, we make the assumption that the density of the gas near the BH scales proportionally to the typical density of the ISM, and is inversely proportional to the mass loading factor  $\beta$  as feedback from star formation is supposed to remove gas from the innermost regions of the galaxy. As discussed, in this study, we do not model the ISM explicitly, but we can make an educated guess on how its density scales with the main ingredients of our model. By assuming that the ISM stratifies in a disc with a radially constant thickness, we write its density as  $\propto M_{\text{ISM}}/R_{\text{ISM}}^2$ . Simple treatments for these quantities are  $M_{\text{ISM}} \propto M_h$  and, in a scenario where the halo angular momentum sets the size of the disc (Fall & Efstathiou 1980; Mo, Mao & White 1998),  $R_{\text{ISM}} \propto r_h \propto M_h^{1/3} \Delta_z^{-1}$  (see Posti et al. 2019b, for a more detailed treatment of disc sizes). With these assumptions,  $\rho_{\text{BH}}$  can be finally written as

$$\rho_{\text{BH}} \sim \rho_{\text{BH},0} \left( \frac{M_h}{10^{12} M_\odot} \right)^{\frac{1}{3}} \beta^{-1} \Delta_z^2 \quad (\text{B8})$$

where the normalization  $\rho_{\text{BH},0}$  is a free parameter.

Our expression for  $\rho_{\text{BH}}$  follows the prescription of B17 and is meant to capture plausible variations in the central gas density, but we stress that different prescriptions can be adopted. For instance, we experimented using  $M_{\text{ISM}} \propto M_{\text{cool}}$ , finding results perfectly compatible with our current implementation. We also tried a more straightforward approach with  $\rho_{\text{BH}} \propto M_{\text{cool}}$  finding similar results, except for a somewhat larger slope in the SHMR in the high-mass range. All considered, our results do not depend significantly on our prescription for  $\rho_{\text{BH}}$ .

As  $M_h$  grows with time, feedback from star formation becomes increasingly less efficient (equation B4) and  $M_{\text{BH}}$  would rapidly diverge if there were no mechanisms that prevented inflow, such as AGN feedback. In our model, we implement a ‘preventative’ AGN feedback recipe (e.g. Zinger et al. 2020), where the energy released by the BH counteracts gas cooling and accretion on to the galaxy.

A BH radiates away a fraction  $\epsilon_r$  of its accreted rest-mass energy providing a luminosity  $L_{\text{AGN}} = \epsilon_r \dot{M}_{\text{BH}} c^2$ ,  $c$  being the speed of light. Since only a fraction  $\epsilon_f$  of such luminosity couples with the gas, the AGN feedback energy rate  $\dot{E}_{\text{BH}}$  will be

$$\dot{E}_{\text{BH}} = \epsilon_f L_{\text{AGN}} = \epsilon_r \epsilon_f \dot{M}_{\text{BH}} c^2. \quad (\text{B9})$$

As commonly done in the literature, we set  $\epsilon_r = 0.1$  (e.g. Soltan 1982; Marconi et al. 2004; Davis & Laor 2011) and treat  $\epsilon_f$ , the so-called ‘BH feedback efficiency’, as a free parameter of our model.

The BH heats the surrounding gas at a rate given by equation (B9). In principle, a detailed calculation of the balance between heating and cooling rates would be required to model self-consistently the physics of gas accretion on to the galaxy. However, this is not a trivial task, given that we ignore both the scale over which the AGN energy is transferred to the gas and the way by which baryons redistribute within the halo after the heating and cooling processes. We therefore adopt a simplified approach, similar to those often adopted in the literature (e.g. Bower et al. 2017; Chen et al. 2020), that aims at capturing the effects of this balance integrated over the entire galaxy lifespan. We assume that the energy output specified by equation (B9) is accumulated during the lifespan of the BH with no significant energy loss. At each time-step, the BH energy output accumulated up to that epoch,  $E_{\text{BH}}(t)$ , is compared to the gravitational binding energy of the gas within the cooling radius of the system, given by

$$E_{\text{cool}} = 4\pi G \int_0^{r_{\text{cool}}} \rho_{\text{gas}}(r) M_h(< r) r dr, \quad (\text{B10})$$

where  $\rho_{\text{gas}}(r)$  is the gas density profile, which we assume to be NFW-like, and  $M_h(< r)$  is the enclosed halo mass. We impose  $E_{\text{BH}}(t) \leq E_{\text{cool}}(t)$ , so that the implemented mass accretion on to the BH is given by the minimum between equation (B6) and the value required for  $E_{\text{BH}}(t)$  to be equal to  $E_{\text{cool}}(t)$ . The physical justification for this choice is that, at any given time, the shell of cooling circumgalactic gas that produces an accretion rate equal to  $\dot{M}_{\text{cool}}$  is located – by definition – at  $r = r_{\text{cool}}$ ; thus the BH needs to heat all baryons within this radius in order to prevent the cooling material from accreting on to the galaxy. Since  $E_{\text{BH}}$  is an integrated quantity, at early times  $E_{\text{BH}} \ll E_{\text{cool}}$ , and the BH population can grow unimpeded following equation (B6) and (B8). Growth rates decrease dramatically when BHs enter the self-regulated, binding energy-limited accretion phase. Examples of BH mass built-up are given in Section 4.1.

A key choice that we make is that, at times when the BH is in the self-regulated phase, we also stop the stellar mass growth. In other words, AGN-driven feedback in our model has two main effects: it quenches star formation and regulates BH accretion. In principle, this phase is not permanent, given that at subsequent times the halo accretes new material and the gas cooling proceeds, effectively increasing  $E_{\text{cool}}$ . In practice though, as we discuss in the main text, we find that once a BH enters the self-regulated phase it never leaves it, and star formation remains suppressed for the rest of the galaxy lifetime.

This paper has been typeset from a  $\text{\LaTeX}$  file prepared by the author.